Development and Characterization of a Field-of-View Background Model for the High Energy Stereoscopic System

Master's Thesis in Physics

Presented by
Christopher Sobel

May 9, 2018

Erlangen Centre for Astroparticle Physics
Friedrich-Alexander-Universität Erlangen-Nürnberg

Supervisor: Prof. Dr. Stefan Funk

Abstract

The aim of this thesis was the development of a field-of-view (FoV) background model for the High Energy Stereoscopic System (H.E.S.S.) which is an array of Imaging Atmospheric Cherenkov Telescopes (IACTs). The subtraction of the background of cosmic-ray induced air showers is a major challenge for such ground-based γ-ray telescope systems. Hence providing an estimate of these background events is of crucial importance. To this purpose 11986 observational runs of the H.E.S.S. I experiment with a total observation time of 5265 h were grouped in bins of zenith and azimuth angle eventually resulting in the creation of 26 independent and unique 3D background models (i.e. energy and spatial resolution). These were stored in tables using the FITS format allowing to be used with open-source analysis tools. Unlike common other background estimation techniques the FoV background model is applicable to complex field of views like very extended sources, areas containing multiple overlapping sources and regions with diffuse γ-ray emission. The subsequent analysis of the model concerning its spatial shape and energy spectrum lead to satisfactory results. Furthermore the agreement of the created background model with a set of 90 observational runs taken on the active galaxy PKS 2155-304 was investigated. By applying a log-likelihood fit an overall background normalization factor of $\Phi = 1.009 \pm 0.006$ was obtained, proving the model to fit well to the selected run data.

Kurzfassung

Das Ziel dieser Arbeit war die Entwicklung eines Field-of-View (FoV) Hintergrundmodells für das High Energy Stereoscopic System (H.E.S.S.), bestehend aus Abbildenden Tscherenkow-Teleskopen (IACTs) zur Untersuchung kosmischer Gammastrahlung. Eine große Herausforderung für solch erdgebundenen Teleskopsysteme liegt in der Subtraktion des Hintergrunds von Luftschauern, die von kosmischer Strahlung herrühren. So ist es von großer Bedeutung, eine Abschätzung dieser Hintergrundereignisse geben zu können. Hierzu wurden 11986 Beobachtungen des H.E.S.S. I Experiments mit einer Gesamtbeobachtungszeit von 5265 h als Datengrundlage herangezogen und gemäß ihres Zenit- und Azimutwinkels gruppiert. Diese Einteilung resultierte in der Entwicklung von 26 unabhängigen 3D Hintergrundmodellen (Energie- und räumliche Auflösung), welche in Tabellen mit FITS Format gespeichert wurden und somit mit open-source Analyseprogrammen genutzt werden können. Im Gegensatz zu anderen gängigen Methoden zur Hintergrundabschätzung ist das FoV Hintergrundmodell auf komplexe Gesichtsfelder anzuwenden. Diese umfassen etwa stark ausgedehnte Quellen, Regionen mit diffuser Gammastrahlenemission sowie auch mehrere sich überlappende Quellen. Die folgende Analyse der räumlichen Verteilung des erstellten Modells und seines Energiespektrums zeigte zufriedenstellende Ergebnisse. Des Weiteren wurde die Übereinstimmung des Hintergrundmodells mit einem Satz von 90 Beobachtungen der aktiven Galaxie PKS 2155-304 untersucht. Mit Hilfe der Log-Likelihood-Methode ergab sich für diesen Datensatz ein Normierungsfaktor von $\Phi = 1,009 \pm 0,006$. Dies stellt eine gute Übereinstimmung des Modells zu den ausgewählten Beobachtungen dar.

Contents

1 Introduction

Astronomy is often being referred to as the oldest of the natural sciences. It involves the study of the origin and evolution of celestial objects and phenomena. With already early civilizations in recorded history methodically observing the night sky, astronomy can be dated back to antiquity.
Despite its far-reaching history, astronomy was restricted to the narrow waveband of optical light for the longest time. Beginning with ancient people using the naked eye, it was the invention of the telescope around 1600 that allowed to observe much fainter objects. Only after successive technological progress in the 20th century, also other non-optical wavebands became accessible for astronomers. Today observations in all ranges of the electromagnetic spectrum are being made. The studies beyond the optical waveband are of great importance as they vastly expand the knowledge and understanding of Galactic as well as extragalactic sources and the universe itself.
The relevant part of the electromagnetic spectrum for this thesis is the one above 100 GeV. Photons in this range are called very-high-energy (VHE) γ rays and can carry energies up to the 100 TeV regime. Since these photons can't be created thermally in celestial systems, they are believed to originate from secondary mechanisms of highly energetic electrons and protons. As opposed to these charged particles, γ rays aren't affected by intra- and extragalactic magnetic fields through the Lorentz force. Thus they follow a straight path and can easily be traced back to their source.
Since γ rays coming from space are absorbed by interactions with Earth's atmosphere they can't be detected directly by ground-based telescopes. One solution is the use of space observatories performing observations from Earth orbit like the Fermi Gamma-ray Space Telescope (FGST). Another approach is to utilize an indirect detection mechanism with ground-based Imaging Air Cherenkov Telescopes (IACTs) like done in the High Energy Stereoscopic System (H.E.S.S.). Here an array of IACTs is detecting Cherenkov light emitted by air showers in the atmosphere which each originate from a primary γ-ray photon.
A major challenge for ground-based γ-ray telescope systems is the subtraction of the background. This background consists of cosmic-ray induced air showers which obviously shall not be taken into account when observing and analyzing γ-ray sources. Thus providing a suitable background model is highly relevant when trying to control systematic effects of IACTs. There are several different types of such models,

each with their own approaches and advantages. Two common background determination techniques are the ring and the reflected-region method which will be presented in section 3.4. Both of these techniques are well applicable concerning γ-ray point sources, however quickly reach their limits when it comes to estimating backgrounds for extended sources. Another possibility is the so-called field-of-view (FoV) background model. Due to its different approach this method also allows for background estimations for more complex field of views. Thereby the FoV background model offers great advantages when dealing with very extended sources, regions containing multiple overlapping sources and areas with diffuse γ-ray emission like, e.g., the Galactic plane. The aim of this master thesis was the development and characterization of such a FoV background model using data from the H.E.S.S. experiment.
The thesis is structured as follows. First the relevant fundamentals of γ-ray astronomy will be presented in chapter 2, covering both cosmic and γ-radiation and their production mechanisms. Moreover the ground-based detection technique of γ rays using IACTs will be examined including the underlying physical processes in the atmosphere. Chapter 3 will give an overview of the H.E.S.S. experiment covering its design and operating principle. In addition two of the common background model methods will be introduced, namely the ring and reflected-region techniques. Chapter 4 will deal with the basic principles of a FoV background model and the creation of the model developed for this thesis. The characteristics of this model will be closely examined in the following chapter 5. To this end, the spatial distribution of the background model as well as its spectra will be analyzed in detail. Additionally a set of H.E.S.S. observations of the γ-ray source PKS 2155-304 will be used to check the agreement with the created background model. Eventually chapter 6 will briefly summarize the results of this thesis and give an outlook of possible ensuing steps.

2 γ-Ray Astronomy

In this chapter the essential topics and principles of γ-ray astronomy relevant for this thesis shall be elucidated. At first cosmic rays and γ rays with their origins and different characteristics are introduced. Afterwards the basic principles of γ-ray detection are examined more closely, providing the fundamentals for the following chapters.

2.1 Cosmic Radiation and Cosmic γ Radiation

After the discovery of radioactivity in the late 19th century it was believed that the observed ionization of the air was caused by this newly explored phenomenon. The accepted opinion was that the radiation of radioactive elements in the ground was responsible for this ionization. Thus the ionization rate of air was expected to decrease with greater altitudes. In 1912 however Victor Franz Hess made a remarkable discovery that both earned him a Nobel Prize in Physics in 1936 and was the birth of cosmic-ray physics. Equipped with three electrometers Hess underwent several free balloon flights up to altitudes of 5300 m on which he measured the ionization rate of air. Contrary to the predominating opinion he found that the ionization rate actually increased at rising altitudes. By doing a balloon ascent during a near-total eclipse he was able to rule out the sun as the possible radiation's source. This made him conclude, that there had to be a radiation of very great penetrating power entering the atmosphere from above [16].
Today we know that this cosmic radiation is composed of highly energetic charged particles within the energy range $10^9\,\mathrm{eV} \leq E \leq 10^{20}\,\mathrm{eV}$. Roughly 90% of these particles are protons and about 9% are α-particles, i.e. helium nuclei [7]. The rest consists of even heavier nuclei or electrons. The all-particle spectrum of cosmic rays can be described by a power law $\mathrm{d}N/\mathrm{d}E \propto E^{-\Gamma}$ with the spectral index Γ. In figure 2.1.1 the cosmic-ray flux is displayed over the energy in double-log depiction. With the so-called knee at $\sim 10^{15}\,\mathrm{eV}$ and the ankle at $\sim 10^{19}\,\mathrm{eV}$ there are two apparent features. Above the knee the spectral index changes from $\Gamma = 2.7$ to $\Gamma \sim 3.1$ until the ankle above which the spectral index changes back to $\Gamma = 2.7$ again.
Apart from the cosmic radiation there also exists a non-charged counterpart with the cosmic γ-radiation. The term γ ray generally refers to photons carrying energies above 100 keV. However the γ rays relevant for this thesis are those within the energy range $100\,\mathrm{GeV} \leq E \leq 100\,\mathrm{TeV}$. These so-called very-high-energy (VHE)

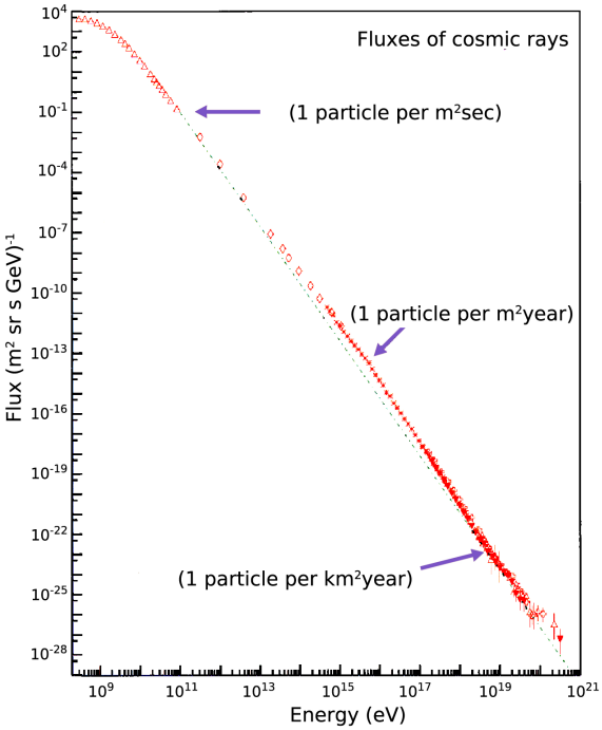

Figure 2.1.1: Cosmic-ray flux as a function of the energy. [7]

γ rays are of cosmic origin and consequently of great importance as they may help to reveal sources of cosmic rays. In case of hadronic emission (see 2.1.2) it is very likely that a source of cosmic rays also produces γ rays. Unlike charged particles these γ rays can be easily traced back to their source since they aren't affected by magnetic fields and thus travel on straight paths. In the following the different possible origins of both cosmic and γ rays will be presented.

2.1.1 Origin of Cosmic Rays

In general the possible sources of cosmic rays are distinguished between Galactic and extragalactic ones. The general assumption is that the cosmic rays below the knee are of Galactic origin, whereas for higher energies, especially above the ankle, the contribution of extragalactic sources to the spectrum is believed to be dominant. This can be explained by the fact that the insufficiently strong Galactic magnetic field is not able to contain particles inside the Galaxy which exceed a certain energy.
As of today the mechanisms by which cosmic rays are accelerated aren't fully re-

solved, however there is strong evidence for potential sources. It is assumed that compact objects with jets like active galactic nuclei (AGNs) mainly contribute to the high-energy part of the spectrum. Cosmic rays below the knee in turn are believed to be produced by a single mechanism and potentially just a single source class like remnants of supernova explosions (SNRs) [11]. The physical process of particle acceleration in shock fronts like they occur in SNRs is fairly well understood and generally known as first order Fermi acceleration. Further information on this topic are provided in reference [13].

2.1.2 Origin of Cosmic γ Rays

The production mechanisms of γ rays can be divided into three groups: Leptonic emission, hadronic emission and dark matter decay or annihilation. The basic principles of these processes shall be elucidated more closely in the following.

Leptonic Emission

The two contributing effects in the category of leptonic emission are synchrotron radiation and Inverse Compton (IC) scattering. The involved particle responsible for emission in these leptonic scenarios is the electron.
Synchrotron radiation is emitted when charged particles of relativistic speed are subject to radial acceleration, i.e. perpendicular to their velocity. Thus highly energetic particles like cosmic rays can emit synchrotron photons when being deflected by a magnetic field B. Considering isotropically distributed pitch angles and a monoenergetic population of electrons with energy E_e, the energy of emitted synchrotron photons is calculated as [11]

$$E_{\mathrm{sync}} = 0.2 \frac{B}{10\,\mu\mathrm{G}} \left(\frac{E_e}{1\,\mathrm{TeV}} \right)^2 \mathrm{eV}. \tag{2.1}$$

Inverse Compton scattering describes the scattering of a highly energetic electron with a low energy photon. This effect allows photons from the cosmic microwave background for example to be scattered to very high energies leading to a broad spectral distribution of γ-ray photons. When considering monoenergetic electrons again, the IC scattering on a population of target photons results in a distribution that peaks at [11]

$$E_{\mathrm{IC}} = 5 \times 10^9 \frac{E_{\mathrm{ph}}}{10^{-3}\,\mathrm{eV}} \left(\frac{E_e}{1\,\mathrm{TeV}} \right)^2 \mathrm{eV}. \tag{2.2}$$

Hadronic Emission

This channel includes the hadron-induced component of γ rays. Relativistic protons or nuclei interact with interstellar material in inelastic collisions, creating secondary pions. Especially the neutral pions π^0 are of interest, as they predominantly decay into two photons, resulting in the interaction chain

$$pp \rightarrow \pi^0 \rightarrow \gamma\gamma.$$

Because of its short lifetime of $\sim 10^{-17}\,\mathrm{s}$ the π^0 almost immediately decays after its production. With roughly 67.5 MeV, the minimum energy of the resulting γ rays in that decay channel corresponds to half of the neutral pion's rest mass.

Dark Matter Decay/Annihilation

The remaining channel potentially contributing to the production of γ rays is dark matter annihilation or decay. Dark matter is a hypothetical type of matter that hasn't been observed directly since it doesn't emit or interact with electromagnetic radiation. However its existence and properties are inferred from deviations from expected galaxy rotation curves or gravitational lensing effects. One promising model for the composition of dark matter assumes the existence of weakly interacting massive particles (WIMPs). In supersymmetric models the lightest of these particles (often the neutralino) is typically predicted to annihilate into heavy final states like $b\bar{b}$, $t\bar{t}$, ZZ, W^+W^- etc. Dominated by the already introduced hadronic emission due to the decay of secondary mesons, all of these channels provide very similar spectra of γ rays.

2.2 Detection of γ Rays

As already pointed out in the introduction, γ rays can't be directly detected on the ground, since they are completely absorbed due to interactions in the Earth's atmosphere. Consequently direct detection can only take place using space observatories in Earth orbit, which is a reasonable choice for γ-ray energies below $\sim 10\,\mathrm{GeV}$. Since the γ-ray flux steeply declines with higher energies however, the rather small detection area of such satellite experiments makes it increasingly difficult to detect photons exceeding that energy. Accordingly the ground-based Imaging Air Cherenkov Telescopes (IACTs) come into play for those higher energies. IACTs use an indirect detection mechanism exploiting the atmosphere as detector material. As a γ ray enters the atmosphere it interacts and generates secondary particles forming a so-called air shower. The Cherenkov light emitted by those secondary particles is then detected by the IACTs, making it possible to

reconstruct direction and energy of the primary incident γ ray. In this section the generation and properties of air showers, both induced by γ rays and hadrons, will be discussed. After presenting the physics behind Cherenkov radiation the Imaging Atmospheric Cherenkov Technique will be examined more closely.

2.2.1 Air Shower Formation

When a high-energy cosmic particle hits the Earth's atmosphere it interacts with atoms and molecules creating secondary particles. Given a high-enough primary energy also the secondary particles undergo interactions, ultimately resulting in an extensive particle cascade, commonly referred to as an air shower. The characteristics of such air showers strongly depend on both the type of the primary particle and its initial energy. Before looking at the different types of air showers the main interaction processes leading to the development of such showers shall be briefly discussed in the following.

Bremsstrahlung describes the electromagnetic radiation produced when a charged particle is decelerated in the Coulomb field of another charged particle. Thus if an electron is deflected by the Coulomb field of an atomic nucleus it loses some of its energy leading to the emission of bremsstrahlung in form of photons. This effect is most likely to be observed with light primary particles like electrons or positrons since the energy loss is inversely proportional to the particle's mass squared.

Pair Production describes the creation of a particle-antiparticle pair from a photon. This effect can only occur in the Coulomb field of another particle allowing for both energy and momentum to be conserved. Moreover the initial energy of the photon has to be at least as high as the total rest mass of the created particles. Consequently the photon energy threshold for the creation of an electron-positron pair is $E_\gamma = 1.022\,\mathrm{MeV}$.

Hadronic interactions involve the scattering of a hadron like a proton on atmospheric nuclei. Considering cosmic rays with sufficient energy the nuclei involved mostly break apart resulting in various nuclear fragments and subatomic particles like pions.

One can distinguish between electromagnetic and hadronic air showers, depending on the type of primary particles. With the main interaction processes having been introduced now these two different types of air showers with their distinct characteristics shall be examined more closely.

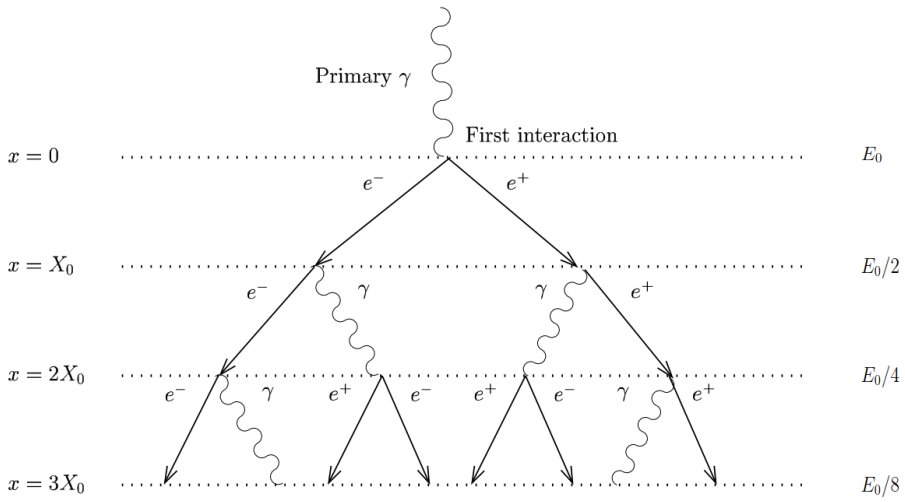

Figure 2.2.1: Schematic model of the development of an electromagnetic air shower according to Heitler. [10]

Electromagnetic Showers

When a particle carrying high enough energy interacts with matter via electromagnetic processes an electromagnetic shower develops. If a γ-ray photon enters the atmosphere it interacts with a molecule resulting in the production of an electron-positron pair. Electron and positron in turn generate further photons again through the effect of bremsstrahlung and so on. The alternation of these two processes leads to an exponential growth of secondary particles forming an electromagnetic shower (see figure 2.2.1). The involved particles lose energy due to both particle production mechanisms and ionization. Once the electron/positron energy falls below a critical energy E_c ionization becomes the dominant effect. From there on no new secondary particles are created, causing the air shower to die out eventually.
A simple model explaining the characteristics of the shower development was first introduced by Heitler in 1954 [15]. With only pair production and bremsstrahlung being considered, energy losses due to ionization are neglected in this model. It also assumes that the energy of a particle is equally distributed among the created secondary particles. For simplicity the radiation length for both pair production and bremsstrahlung are considered to be the same. Starting with a primary γ ray with energy E_0 entering Earth's atmosphere, the total number of particles N after m radiation lengths X_0 is given by

$$N(m) = 2^m \tag{2.3}$$

with each of these particles carrying the energy

$$E(m) = E_0 \cdot 2^{-m}. \tag{2.4}$$

The number of particles increases steadily, reaching its maximum at the critical energy E_c.

$$E(m_{\max}) = E_0 \cdot 2^{-m_{\max}} = E_c \quad \rightarrow \quad m_{\max} = \frac{\ln(E_0/E_c)}{\ln(2)} \tag{2.5}$$

After $m_{\max}$ radiation lengths the electromagnetic shower reaches its maximum with the total number of particles being

$$N_{\max} = N(m_{\max}) = \frac{E_0}{E_c}. \tag{2.6}$$

Despite relying on just a few basic assumptions the model of Heitler features the main properties of electromagnetic showers like the exponential increase of particles until E_c or the direct proportionality between the maximum number of particles $N_{\max}$ and the primary energy E_0 of the initial γ ray.

Hadronic Showers

Hadronic air showers are initiated by protons, neutrons or atomic nuclei entering the atmosphere. As opposed to electromagnetic showers, the interactions taking place are much more complex leading to the development of both hadronic and electromagnetic sub-showers. When a hadron interacts with an air molecule strong interaction processes are dominant. Considering a primary proton mainly mesons like pions and kaons but also other nuclei or even hyperon states are created (see figure 2.2.2).
The charged pions ($\pi^{\pm}$) and kaons ($K^{\pm}$) have a lifetime of $\sim 10^{-8}$ s and either decay or interact inelastically with atmospheric nuclei generating hadronic sub-showers. The most probable decay products are muons ($\mu^{\pm}$) and neutrinos ($\nu_\mu/\bar{\nu}_\mu$). The latter barely interact with matter flying straight through Earth. The muons either decay in electrons and neutrinos or reach the Earth's surface as they don't interact strongly and mainly lose energy through ionization processes.
The neutral pions (π^0) decay into two photons almost instantly after their creation. As explained previously the photons then initiate electromagnetic sub-showers due to alternation of pair production and bremsstrahlung.
With these underlying complex multi-particle processes hadronic showers contain more variances and less regularity than electromagnetic showers. As a result of the inelastic strong interactions also the lateral spread of hadronic showers is significantly larger than the lateral spread of electromagnetic ones as will be shown in the following section.

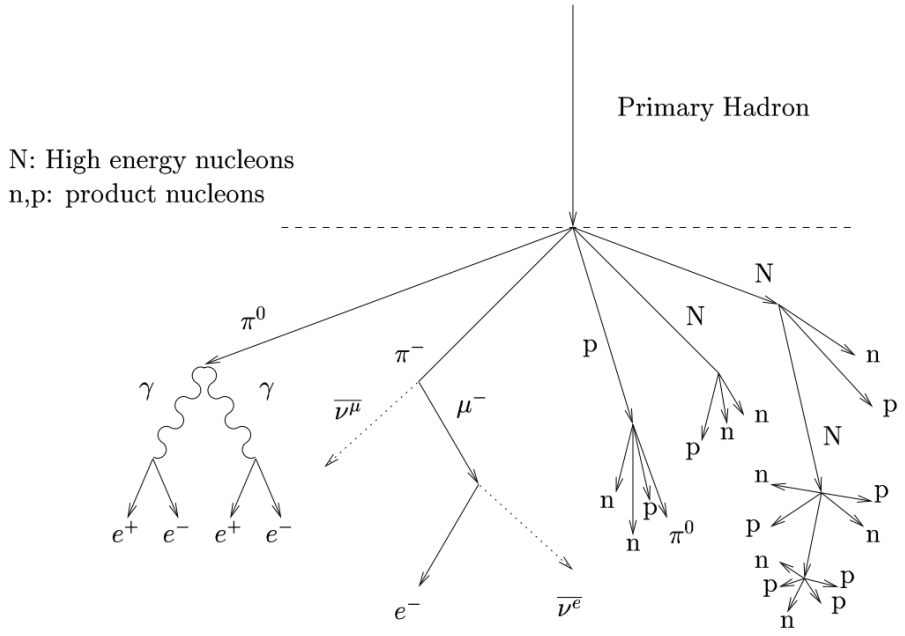

Figure 2.2.2: Schematic model of the development of a hadronic air shower. [10]

2.2.2 Cherenkov Radiation

When a charged particle travels through a dielectric medium the molecules of this medium are polarized due to the particle's electric field. The exchange of information happens with the speed of light in that medium $c_n = c/n < c$, with the refractive index n of the medium and c the speed of light in vacuum. If a particle travels with the velocity $v < c_n$, all of the surrounding molecules take note of its electric field and dipoles are aligned correspondingly until the particle has passed and they disappear again. However if the particle travels with a velocity $v > c_n$ it passes the surrounding molecules faster than the speed with which the information of its electrical field is being transfered to them. The ensuing depolarization of the disturbances left behind result in the emission of electromagnetic radiation forming a wave-front with linear propagation (see figure 2.2.3). This so-called Cherenkov radiation typically has a wavelength in the range between 350 and 550 nm and thus can be detected optically.
The opening angle θ_c (Cherenkov angle) of the wave-front can be calculated via

$$\cos(\theta_c) = \frac{c_n \cdot \Delta t}{v \cdot \Delta t} = \frac{c_n}{v} = \frac{c}{n \cdot v}. \tag{2.7}$$

Since $\cos(\theta_c)$ can't be greater than 1, Cherenkov light only is emitted if the particle's velocity exceeds the speed of light in the considered medium, satisfying

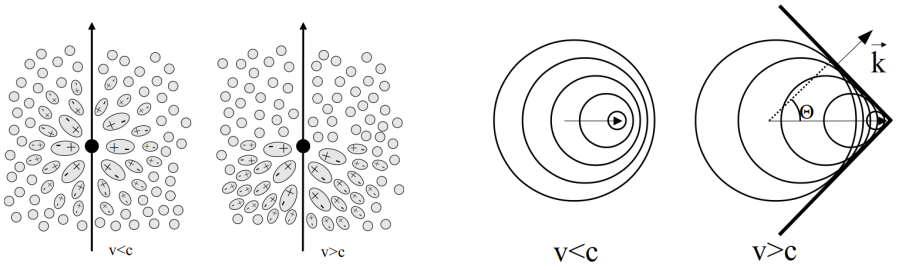

Figure 2.2.3: **Left:** Polarization of a dielectric medium induced by a charged relativistic particle. **Right:** Construction of a Cherenkov wave-front. [9]

$v > c_n = c/n$. In case of an ultra-relativistic particle ($v \approx c$) the maximum opening angle is given by

$$\theta_{c,\max} = \arccos\left(\frac{1}{n}\right). \tag{2.8}$$

With the density of air molecules increasing with decreasing height, also the refractive index n of air and consequently the opening angle increase. Since the secondary particles in electromagnetic showers are mainly emitted in the direction of the primary particle, the Cherenkov light forms a cone around the path of the primary particle. Considering an incident electron with an energy of 1 TeV the Cherenkov angle takes values of $\sim 1°$, resulting in a Cherenkov cone with a diameter of

$$d = 2h \cdot \tan(\theta) \approx 2h\theta \tag{2.9}$$

on the ground. The typical height h of the shower maximum in this scenario is $\sim 8\,\text{km}$ [14] leading to a Cherenkov cone diameter of $\sim 280\,\text{m}$ on the ground.
As pointed out in the previous section hadronic showers have a larger lateral spread and more irregularities as opposed to electromagnetic showers. These differences become apparent when looking at figure 2.2.4, where the simulated Cherenkov light production for different primary particles is displayed in longitudinal direction. In figure 2.2.5 the lateral distribution of simulated Cherenkov light is shown. The light cone of the γ-ray induced electromagnetic shower has a homogeneous distribution with slightly decreasing intensity towards the shower axis. The Cherenkov cones of the hadronic showers differ distinctly as the secondary particles experience a larger spreading. Due to the creation of electromagnetic sub-showers the emitted Cherenkov radiation shows much more fluctuations leading to an irregular shape.

2.2.3 Imaging Atmospheric Cherenkov Telescope

The ground-based detection of high-energy γ rays relies on Imaging Atmospheric Cherenkov Telescopes (IACTs). They work by imaging the Cherenkov radiation

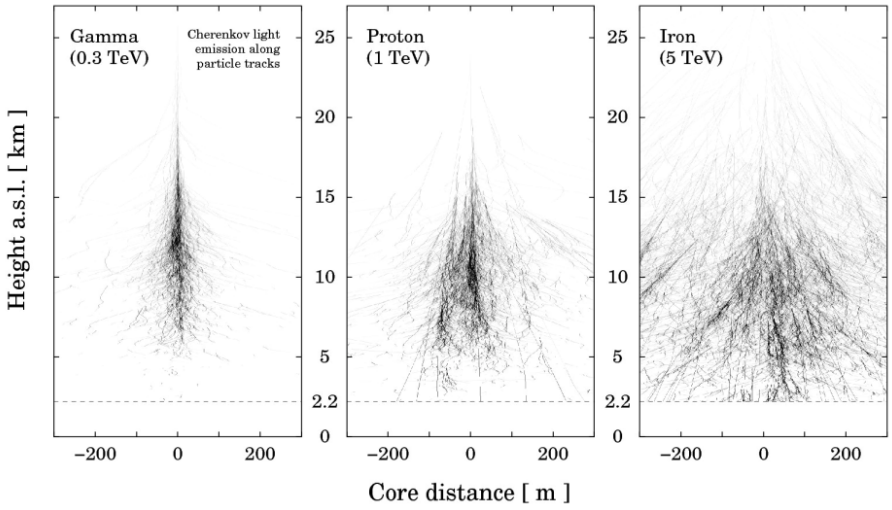

Figure 2.2.4: Simulations of Cherenkov light production for different primary particle examples. Darkness of the particle tracks shown increases with increasing emission of Cherenkov light. [5]

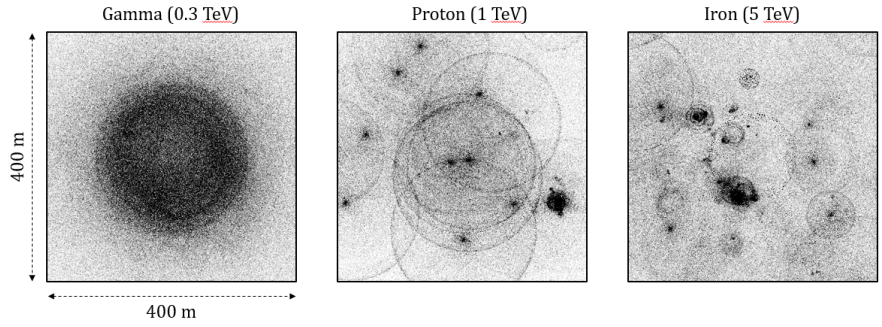

Figure 2.2.5: Simulated lateral distribution of Cherenkov light. [4]

emitted by the cascade of relativistic secondary particles in air showers. The basic elements of IACTs and the rationale of the applied imaging atmospheric Cherenkov technique shall be briefly presented in the following.
Considering a 1 TeV primary γ ray just $\sim$ 100 photons per m^2 hit the ground, illuminating an area of about 260 m diameter. The photons created in one shower all arrive within a time window of only a few nanoseconds. If an IACT is located somewhere inside that illuminated area the Cherenkov light is collected by its mirror and reflected onto a camera. Thus the detection area is given by the whole illuminated area of the Cherenkov light cone. With $\sim 50000\,\mathrm{m}^2$, it is 5 orders of

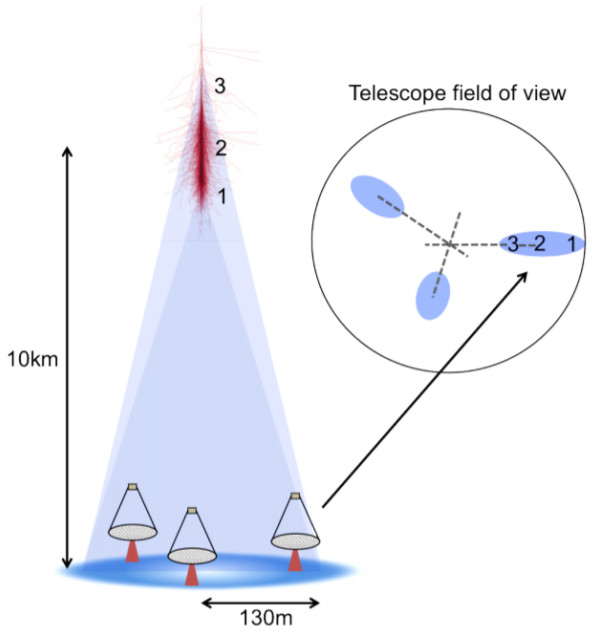

Figure 2.2.6: Illustration of the stereoscopic imaging technique. [18]

magnitude larger than the detection area of a typical satellite experiment. Despite the decreasing flux towards higher energies this allows IACTs to observe γ rays in the TeV-regime on reasonable time scales.
Due to the small photon density of air showers the commonly segmented mirror is build as large as possible. By maximizing the collection area the energy threshold of the system is lowered. Because of the small time window in which the photons are arriving on the ground it is essential to have fast electronics and detectors being able to distinguish the faint Cherenkov light flashes from night-sky background fluctuations. In today's telescopes the camera commonly consists of multiple photomultiplier tubes (PMTs) which meet this challenge. They have a nanosecond response time and are able to resolve single photon events.
The image obtained of the air shower is of elliptical shape with the major axis pointing towards the shower axis. Today's experiments commonly make use of stereoscopy, where multiple IACTs are imaging air showers simultaneously (see figure 2.2.6). Each telescope provides a different elliptical image of the shower and the intersection of the major axes gives the arrival direction of the incident γ ray. Also the energy of the primary particle can be deduced as it is related to the intensity of the images.
Observations with IACTs are preferably made in moonless nights and are com-

monly split into runs of $\sim 30\,\mathrm{min}$ in duration during which a fixed point in the sky is targeted. There are two common observation modes that can be applied. The on/off-mode describes a procedure where in one run a γ-ray source of interest is being pointed at (on-run) and in the next run an empty sky region is observed (off-run). Considering a similar background in both the on- and off-runs the signal of the object can be derived by their difference. The fact that half of the observation time is spent on tracking off-regions without any source constitutes a major drawback compared to the so-called wobble-mode. Here the object of interest is in the field of view in every run with the telescope's pointing being offset from the source by typically $0.5°$. Using this method the background for the source region can be estimated from the field of view itself. Thus both the so-called on- and off-data is taken within the same run.

3 The H.E.S.S. Experiment

The High Energy Stereoscopic System (H.E.S.S.) is a ground-based array of imaging atmospheric Cherenkov telescopes being able to detect high-energy γ rays in the range from tens of GeV to tens of TeV. The experiment's name is a tribute to Victor Franz Hess who discovered cosmic rays in 1912. The H.E.S.S. site is located at 1800 m above sea level in Namibia near the Gamsberg, an area well known for its outstanding optical quality. After starting with the first telescope in summer 2002 all four telescopes of Phase I of the H.E.S.S. project were operational in late 2003. A much larger fifth telescope started operating in July 2012, introducing Phase II of the experiment.

3.1 Telescope System

The first four telescopes of H.E.S.S. I have a mirror diameter of 12 m each and are arranged in a square with a side length of 120 m. With greater distance between the telescopes also the angles between the different views increase, resulting in a better stereoscopic view of the observed air showers. Since the illuminated area on the ground of one single shower is about 260 m in diameter a spacing too large however would make it increasingly unlikely for multiple IACTs to be within the same Cherenkov light cone. Thus the applied spacing represents a compromise between large base length necessary for reasonable stereoscopy and the condition that at least two telescopes are hit by Cherenkov light generated by one shower.
The mirror of each telescope consists of 380 round mirror segments made of quartz coated aluminized glass. The focal length of the mirror is 15 m and its facets are arranged in a Davies-Cotton design, granting good imaging also for off-axis rays. Each mirror segment has a 60 cm diameter resulting in a total mirror area of 107 m^2 per telescope [6]. They are focused for an object distance of ~ 10 km which is commonly about the altitude of the maximum of a γ-ray induced air shower. The camera of each telescope is composed of 960 pixels mounted in a hexagonal grid and has a field of view of 5°. Each pixel consists of a photomultiplier (PMT) recording the intensity of the incident light and a Winston cone in front of it. The latter closes the gap between the pixels, collecting and guiding the light into the PMTs which otherwise would have been lost. With the dimensions 160 cm $\times$ 160 cm $\times$ 150 cm the camera reaches a weight of ~ 1 t [8]. Since H.E.S.S. relies on stereoscopic reconstruction of air showers only showers generating images in two or more telescopes

Figure 3.0.1: View of the full H.E.S.S. array with the four 12 m telescopes and the 28 m H.E.S.S. II telescope. [23]

are recorded. Each telescope triggers if a minimum number of pixels within a certain sector measure a signal exceeding a certain threshold within a short time frame on the nanosecond scale. A central trigger system receives the trigger signals from each telescope and only in case of coincident triggers between individual telescopes the data are read out. Otherwise the data are cleared and the readout electronics is ready for the next event [12].
The fifth 28 m-sized telescope (CT5) was added at the center of the four-telescope array. To minimize time dispersion CT5 uses a parabolic mirror shape approximated by a grid of 5×5 planar mirror support segments. It consists of 875 hexagonal facets also made of aluminized glass with a quartz coating and has a focal length of 36 m. Each mirror segment is 90 cm (flat to flat) in size resulting in a total mirror area of $614\,\mathrm{m}^2$. The camera of CT5 follows the design of the four H.E.S.S. I telescopes. It is composed of 2048 pixels and has a field of view of 3.2°. Groups of 16 PMTs are housed in drawers containing the electronics for signal storage, signal digitization, triggering and readout. Despite having the same pixel size like the 12 m telescopes shower images of CT5 have a much better resolution because of the larger focal length. The camera body has the dimensions of $227\,\mathrm{cm} \times 240\,\mathrm{cm} \times 184\,\mathrm{cm}$ weighing $\sim 3\,\mathrm{t}$ [8]. With the addition of CT5 the central trigger system was upgraded, allowing triggering on coincidences between the five telescopes in arbitrary combinations. The typical settings require a coincidence of any two of the telescopes to trigger an image readout. To provide a minimal energy threshold however also showers only registered by CT5 are recorded.

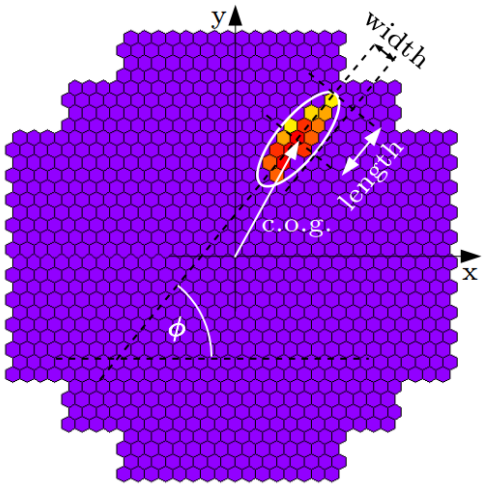

Figure 3.2.1: Cleaned camera image with an overlaid ellipse and geometric interpretation of the Hillas parameters. [19]

3.2 Event Reconstruction

The elliptically shaped images obtained from electromagnetic air showers display the Cherenkov light emitted from secondary particle cascades. Coming from these raw camera images the objective now is to reconstruct the underlying event, i.e. the initial primary particle with its properties like type, energy and direction.
At first the image is cleaned to get rid of pixels with noise signals originating from night sky background or PMT noise. Typically only pixels with an intensity above a threshold of 10 photoelectrons (p.e.) and an adjacent pixel with an intensity above 5 p.e. or vice versa are kept in. All other pixels are assumed to be unrelated to the air shower and set to zero [2].
The remaining ellipse can now be characterized with the so-called Hillas parameters which can be derived from the light intensity distribution in the camera. These parameters, illustrated in figure 3.2.1, correspond to certain geometric properties of the shower image like the length, width and orientation of the ellipse, as well as its center of gravity coordinates and the integrated intensity over all pixels inside (the so-called image size).
Since H.E.S.S. makes use of a stereoscopic observation technique the telescopes' views of the air shower from different angles are utilized for the direction reconstruction. As already pointed out in section 2.2.3 the arrival direction of the incident γ ray can be determined by superimposing the different shower images and intersecting the major axes obtained (see figure 3.2.2). This works since the origin of the primary particle is always located on the major axis of each ellipse. Also the

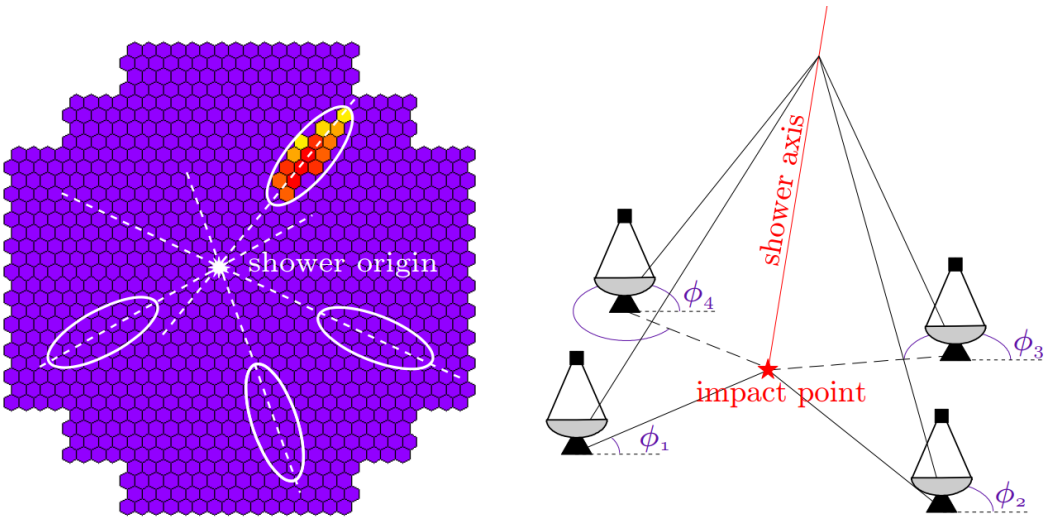

Figure 3.2.2: **Left:** Illustration of stereoscopic reconstruction with superimposed ellipses from four telescopes. **Right:** Principle of the stereoscopic reconstruction of the impact point. [19]

impact point of the shower can be determined in similar fashion (see [17]).
With the direction of the supposed γ-ray photon being identified the energy reconstruction can be performed next. The primary energy depends on the image size, the zenith angle during the observation as well as the distance of the telescope to the impact point (impact distance). For each telescope these parameters are compared to those resulting from Monte-Carlo simulated γ-ray showers which are stored in so-called look-up tables. The reconstructed energy of the event E_{reco} is then calculated as the mean of the energies independently assigned for each telescope. The error of the energy is given by

$$\Delta E = \frac{E_{\mathrm{reco}} - E_{\mathrm{true}}}{E_{\mathrm{true}}} \tag{3.1}$$

with E_{true} the energy obtained from Monte-Carlo simulations. The energy bias is defined as the mean value of ΔE and increases towards lower energies. The smaller the energy of the primary γ ray the less Cherenkov light is emitted and potentially collected by the telescopes. For energies close the threshold of the system this results in much greater statistical fluctuations of the image size as opposed to higher primary energies.

3.3 Gamma-Hadron Separation

IACTs detect both hadronic and γ-ray induced air showers. Since most of the observed showers originate from cosmic rays it is an important objective to suppress these background events as much as possible while on the other hand keeping a maximal number of γ-ray events. A compromise has to be made resulting in several cut criteria that are applied trying to maximize the signal-to-background ratio.
The *local distance cut* reduces the occurrence of truncated images due to the camera edges. Therefore the distance between the center of gravity of the image and the camera center must not exceed a certain threshold. An additional cut ensures the rejection of events if the image size falls below a given value (*size cut*). Hence at the expense of a higher energy threshold images being too faint are sorted out.
The *directional cut* is a cut made on θ^2, the squared angular offset between the reconstructed shower direction and the true direction of the γ-ray source being observed. Looking at the distribution of reconstructed shower directions expressed in units of θ^2 an excess close to zero, corresponding to events coming from source direction, is expected. A cut on θ^2 can now exploit the fact that γ rays travel on straight paths and can be traced back to their source, whereas cosmic rays are affected by magnetic fields hence arriving isotropically on Earth.
The *scaled cuts* are the ones mainly responsible for the suppression of non γ-ray background events. These cuts depend on the relation between the recorded image width w and length l and their expectation value $\langle w \rangle$ and $\langle l \rangle$ along with the standard deviation $\sigma_{\mathrm{w/l}}$ according to γ-ray simulations. For a stereoscopic system with N telescopes the two cut parameters mean reduced scaled width ($MRSW$) and length ($MRSL$) are defined as

$$MRSW = \frac{1}{N} \sum_{i=1}^{N} \frac{w_i - \langle w \rangle (I_i, b_i, \theta)}{\sigma_{\mathrm{w}}(I_i, b_i, \theta)} \tag{3.2}$$

$$MRSL = \frac{1}{N} \sum_{i=1}^{N} \frac{l_i - \langle l \rangle (I_i, b_i, \theta)}{\sigma_{\mathrm{l}}(I_i, b_i, \theta)}. \tag{3.3}$$

As the equations indicate both the mean value and the scatter vary with the image size I, the impact distance b and the zenith angle θ. Cuts on $MRSW$ and $MRSL$ exploit the distinct difference in shape between hadronic and electromagnetic showers, thus making them very effective. In figure 3.3.1 the distributions of $MRSW$ for γ rays and protons from Monte-Carlo simulations are depicted, as well as for real off-source data without any image cuts applied. As expected this comparison shows a good agreement between the measured background and simulated protons. On the other hand there is a distinct separation between the real off-source data and the Monte-Carlo simulated γ rays. The distributions of $MRSL$ show a very

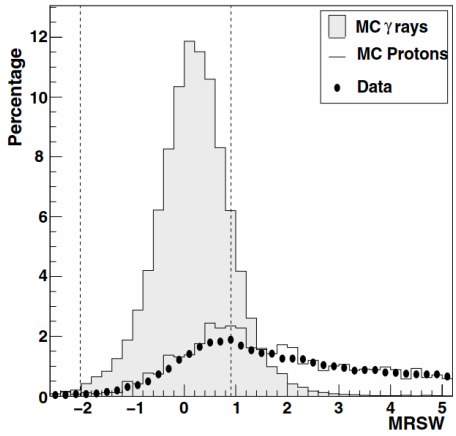

Figure 3.3.1: Distribution of MRSL for Monte-Carlo simulated γ rays, protons and actual off-source data before selection cuts. [2]

similar behavior. This example illustrates that the *scaled cuts* are very suitable to distinguish between hadronic and γ-ray induced showers making them a major contributor in the suppression of background events.

3.4 Background Determination

By applying the cuts described in the previous section the cosmic ray background can be reduced immensely by a factor of ~ 100 in case of a stereoscopic experiment with 100 GeV threshold. However even for a strong point source like the Crab nebula there still remains a signal-to-background ratio on the order of 1:1 [2]. The residual γ-like background mainly consists of hadronic events that happen to meet all cut criteria and to some extent of randomly distributed γ rays originating from collisions of cosmic rays with interstellar gas for example. In order to extract the pure signal from a source the remaining background has to be estimated and subtracted from the data. The so-called γ-ray excess which gives the strength of the source's signal is defined as

$$N_{\text{excess}} = N_{\text{on}} - \alpha N_{\text{off}} \tag{3.4}$$

with N_{on} the number of counts (events) within a defined on-region including the source and N_{off} the number of counts within a background control region off-source. The differences of these two regions concerning solid angle, exposure time t, zenith angle θ or system acceptance A^{γ} are taken into account by the normalization factor

α which is defined as

$$\alpha = \frac{\int_{\text{on}} A^{\gamma}_{\text{on}}(\psi_x, \psi_y, \theta, E, t)\, \mathrm{d}\psi_x\, \mathrm{d}\psi_y\, \mathrm{d}\theta\, \mathrm{d}E\, \mathrm{d}t}{\int_{\text{off}} A^{\gamma}_{\text{off}}(\psi_x, \psi_y, \theta, E, t)\, \mathrm{d}\psi_x\, \mathrm{d}\psi_y\, \mathrm{d}\theta\, \mathrm{d}E\, \mathrm{d}t}. \tag{3.5}$$

The system acceptance represents the probability that a γ-ray-like event is reconstructed with an energy E at a certain position in the telescope's FoV given by ψ_x and ψ_y. It also depends on the zenith angle of the observation and accounts for different exposure times for on- and off-region. In many cases it is a good approximation to assume a radially symmetric behavior of the acceptance. The statistical significance of the obtained γ-ray excess can be derived with a maximum likelihood method [20] and is given by

$$S = \sqrt{2}\left[N_{\text{on}} \ln\left(\frac{1+\alpha}{\alpha}\frac{N_{\text{on}}}{N_{\text{on}}+N_{\text{off}}}\right) + N_{\text{off}} \ln\left((1+\alpha)\frac{N_{\text{off}}}{N_{\text{on}}+N_{\text{off}}}\right)\right]^{1/2}. \tag{3.6}$$

By choosing background regions in a way that $\alpha \ll 1$ commonly a higher statistical significance can be obtained due to the reduction of background fluctuations. This can be achieved for example by choosing larger off- than on-regions which however may also lead to increasing systematic errors. There a various approaches concerning the choice of off-regions each with their own advantages. In the following two of the common background modeling techniques shall be introduced more closely.

Ring Background Model

The ring background model is a method in which the off-region is defined as a ring around the on-region including the source of interest. The torus has a radius of typically 0.5° and an angular size about 7 times larger than the on-region. The number of off-counts N_{off} is calculated by adding up all events lying inside this ring region. Known γ-ray sources within the FoV (besides the one of interest) are excluded from this calculation which is realized by defining exclusion regions. The normalization factor α can be roughly approximated as the ratio of the angular size of the ring to the angular size of the on-region. However there are areas with different offsets from the center of the FoV within the torus. Since the acceptance varies with radial distance from the camera's center this fact has to be accounted for when deriving α by using an acceptance correction function. In figure 3.4.1 (left) the Ring Background method is displayed schematically.

Reflected-Region Background Model

Using the reflected-region background method it is essential to have the on-region positioned offset from the camera's center. This applies for the usual

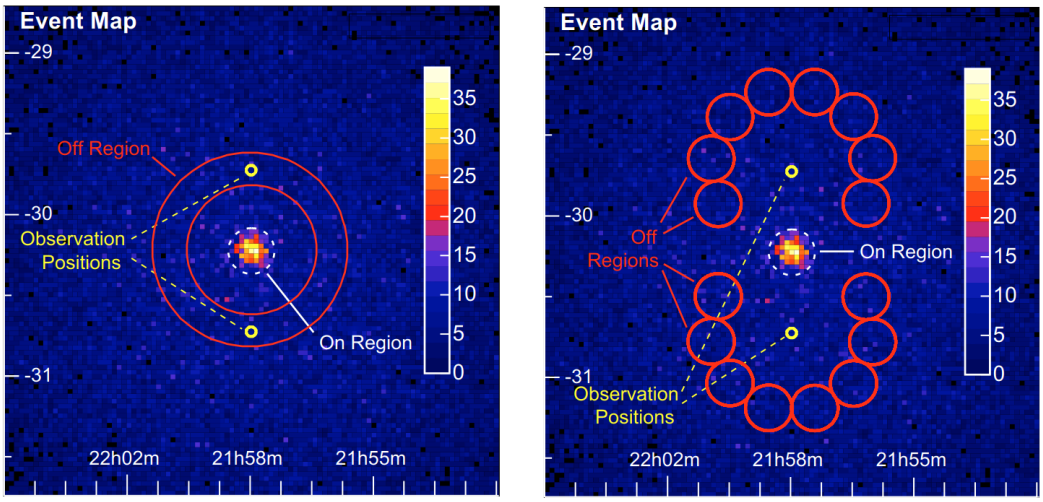

Figure 3.4.1: Count map of γ-ray-like events from 5 h of H.E.S.S. observations of the active galaxy PKS 2155–304 ([1]). Schematic illustration of the ring background method (**left**) and of the reflected-region background method (**right**). [3]

wobble-mode where the source of interest is offset by typically 0.5°. The n_{off} off-regions each have the same angular size like the on-region and are positioned on a circle around the center of the FoV with a radius equal to the wobble offset. The method's name refers to the fact that the on-region is reflected with respect to the pointing position to obtain the off-regions. As many off-regions as possible are fit on that circle without overlapping each other. However a certain minimal distance to the on-region has to be ensured to avoid a contaminated background estimate by poorly reconstructed γ rays. As opposed to the ring background method no acceptance correction has to be applied since on- and off-regions have the same offset from the pointing direction. Thus the acceptance is equal for every region and the normalization factor is simply given by $\alpha = 1/n_{\text{off}}$. This constitutes a major advantage of this method as there is no need for an acceptance function in case of spectral analysis for example. Obviously this only applies under the assumption of a radial symmetry of the acceptance.

4 Development of a Field-of-View Background Model

In the previous section the ring background as well as the reflected-region background model have been introduced. In this chapter another possible technique to estimate the background, the so-called FoV background model, shall be examined more closely. After outlining the basic principles of this method the actual topic of this thesis shall be elucidated, namely the development of such a background model using H.E.S.S. I data.

4.1 Field-of-View Background Model

For the FoV background model the off-region is given by the telecope's entire field of view. By adding up all detected events of numerous runs in the camera's coordinate system and dividing by the exposure time of each pixel a background rate map can be derived. Known γ-ray sources are excluded, ensuring to only take γ-like background events into account. Unlike the ring and reflected-region methods, where a background is determined for a specific on-region, the resulting maps of the FoV background model provide a background estimate for the entire field of view. Optimally a big data set of as many runs as possible is used to reduce statistical fluctuations. Since the system acceptance is strongly dependent on the zenith angle of the telescope's pointing direction the background rate is calculated separately for 13 zenith angle bins. Similarly, observations are grouped in two different azimuth angle bins to account for the varying influences of the Earth's magnetic field on the shower development. The acceptance also depends on the energy of the primary particle. Hence the creation of a so called 3D background model is favorable. Therefore every event's energy is taken into consideration resulting in the construction of a 2D background map for up to 20 energy bins. In contrast to the ring and reflected-region background methods, which are unfavorable when the on-region is too large, the FoV background model can be readily applied to complicated field of views. This constitutes a major advantage of this background determination technique as it is applicable to very extended sources, areas containing multiple overlapping sources and also regions with diffuse γ-ray emission. The crucial difference between the FoV background model and the ring and reflected-region methods lies in the acquisition of the data used to estimate

the background. The latter two models take a single specific run and determine a background estimate for a certain on-region by using the data of the same observation. Hence on- and off-data are always taken from the same run and under the same observation conditions. In case of the FoV background model however the background rate is taken from a model that is based on multiple other runs with similar, but not necessarily identical observational conditions. As opposed to the ring and reflected-region background this adds a systematic uncertainty as the conditions of the run of interest (on-data) may vary from the averaged conditions of the numerous observations used to create the background estimate (off-data).

4.2 Building the Background Model

With the basic principles having been introduced now the FoV background model developed for this thesis and the approaches applied shall be presented in the following. The data used consist of observational runs of the H.E.S.S. experiment all taken in phase I. Since a broad band of diffuse γ-ray emission is located along the Galactic plane only observations off that plane were taken into consideration. This was realized by excluding all runs with a pointing direction within an area of $\pm 60°$ in longitude and $\pm 5°$ in latitude around the Galactic Center. The remaining 11986 observations were then grouped in bins of zenith and azimuth angle to account for the previously explained dependencies of the system acceptance. The bin edges used for the applied grouping are shown in table 4.1 resulting in 26 different observational bins, each representing a particular range of observational attributes.

	Bin Edges [°]													
Zenith	0	10	25	35	42.5	47.5	52.5	57.5	61.5	64	66	68	69.5	90
Azimuth				-90				90				270		

Table 4.1: Bin boundaries for zenith and azimuth angle.

The number of runs varies widely between different zenith angle bins. This can be seen in table 4.2 where the number of runs in each of the predefined bins is shown. The bin numbers in this table correspond to the bin boundaries given in table 4.1. Accordingly zenith bin number 0 corresponds to a zenith angle in the range of $0° - 10°$ and azimuth bin number 1 for example corresponds to an azimuth angle in the range of $90° - 270°$. It becomes apparent that the vast majority of observations was done at rather small zenith angles and hence small energy thresholds. In section 5.1 the correlation between zenith angle and energy threshold will be discussed in more detail.
As a next step all runs within the same observational bin were stacked by adding all events in a Alt/Az-aligned FoV coordinate system. In this specific system the coor-

		Zenith Bin												
		0	1	2	3	4	5	6	7	8	9	10	11	12
Azimuth	0	262	1261	971	573	656	313	205	47	71	30	15	5	0
Bin	1	1010	2802	1475	1029	652	509	64	24	6	3	3	0	0

Table 4.2: Number of runs in each observational bin.

dinates are centered on the array's pointing position with the x-axis being aligned in azimuth and the y-axis being aligned in altitude direction. These directions refer to the horizontal coordinate system which is connected to an observer at a given location on Earth and point in time. It uses the observer's local horizon as the fundamental plane and is expressed in terms of an azimuth and altitude angle. To only account for the γ-like background all events originating from regions of known γ-ray sources were excluded. Thus for every run it was checked in 10 s intervals whether a spatial pixel in the FoV coordinates was exposed or covered by an exclusion region due to a γ-ray source. In the latter case all of the events detected within that time interval and assigned to that pixel were dismissed and not added. Since it was the aim to construct a 3D background model also the energy of the events was taken into consideration resulting in a 3D histogram for every observational bin. Each of the 26 3D histograms, representing an observational bin, contains several 2D background excess maps corresponding to different energy bins respectively. Both the spatial and energy binning were done adaptively depending on the total number of measured events N_{ev} within an observational bin. When exceeding a value of 240000 events a fixed number of $N_{\mathrm{E}} = 20$ energy bins and $N_{\mathrm{s}} = 75$ spatial bins, both in x and y direction, were used. Otherwise the number of bins was reduced to avoid empty bins due to insufficient statistics. The rules applied for the calculation of the number of bins were [22]

$$N_{\mathrm{E}} = \begin{cases} 75 & N_{\mathrm{ev}} \geq 240000 \\ 75 + ((N_{\mathrm{ev}}/1500)//10 - 16) & \text{else} \end{cases} \tag{4.1}$$

$$N_{\mathrm{s}} = \begin{cases} 20 & N_{\mathrm{ev}} \geq 240000 \\ 20 + 3((N_{\mathrm{ev}}/1500)//10 - 16) & \text{else} \end{cases} \tag{4.2}$$

with // being the floor division returning the integral part of a quotient. The observational bins affected by the reduction of energy and spatial bins correspond to the bins with only 30 runs or less in table 4.2. The created background excess maps for every energy bin are all $7.5^\circ \times 7.5^\circ$ in size. For the most common case of $N_{\mathrm{s}} = 75$ this results in a pixel width of 0.1°.
In the next step the number of events per bin in the 3D histograms was translated into a background rate being independent of the binning definition. Therefore each bin content was divided by the width of the respective energy bin, by the spatial

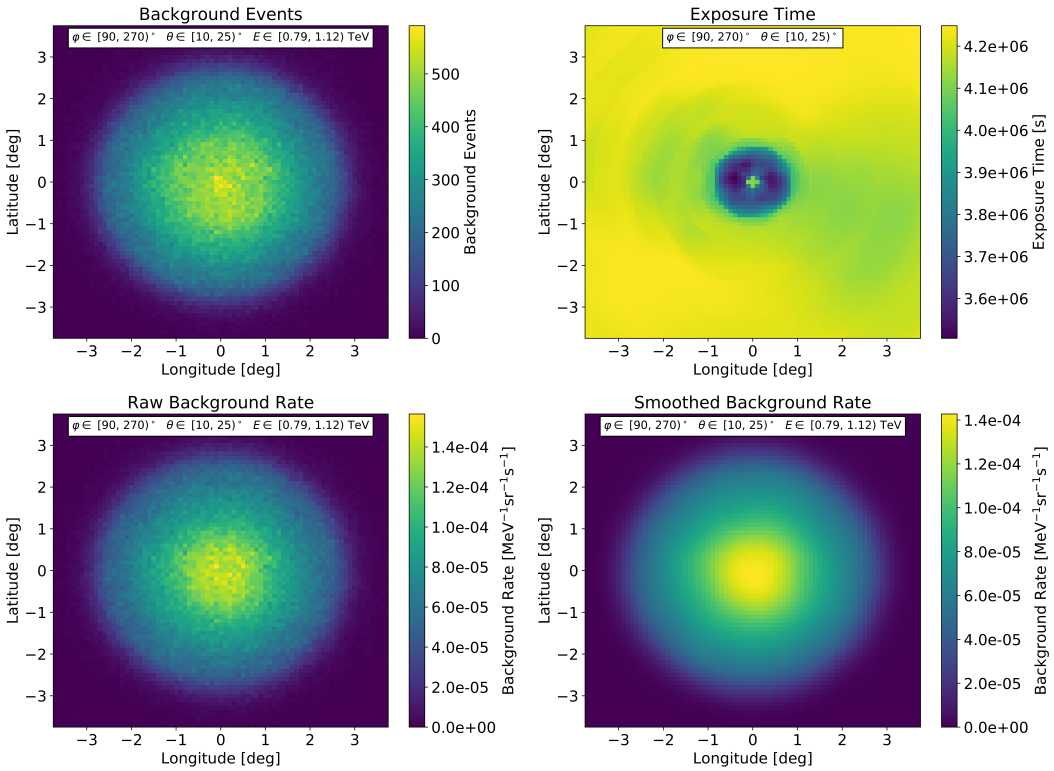

Figure 4.2.1: Different stages in the development of the FoV background model. **Top Left:** Stacked γ-like background events. **Top Right:** Exposure time of each spatial pixel. **Bottom Left:** Derived raw background rate. **Bottom Right:** Final background rate after applied smoothing algorithm.

size of one bin and by the total exposure time of the respective spatial bin. Consequently each bin now represents a background event rate in units of $\mathrm{MeV}^{-1}\mathrm{sr}^{-1}\mathrm{s}^{-1}$. By applying a smoothing algorithm on the obtained 3D histograms as a last step statistical fluctuations were removed as good as possible.
Figure 4.2.1 shows the just described process of the development of the background maps. The example taken refers to the observational bin with a zenith angle $\theta \in [10, 25)^\circ$ and an azimuth angle $\varphi \in [90, 270)^\circ$ as well as an energy $E \in [0.79, 1.21)\,\mathrm{TeV}$. In the top left the summed up events of all 2802 runs within that observational bin and energy range are shown. By dividing each pixel by the corresponding exposure time (top right), the width of the energy bin and the spatial bin size one obtains the so-called raw background rate (bottom left). The distinctive ring-like feature around the center of the FoV in the exposure time map

arises from the commonly applied wobble-mode when observing γ-ray sources. In the bottom right the background rate after the applied smoothing algorithm is displayed. The fluctuations are removed in satisfactory fashion resulting in a smooth, approximately radially symmetric background map.
As a final result 26 independent 3D background models were created, which now can be used to provide a background estimate for any arbitrary observational run. Therefore based on its pointing in zenith and azimuth this run just has to be assigned to the corresponding observational bin, respectively the correct 3D background model originating from various runs with similar pointing direction. The 26 unique background models were stored in tables using the FITS format allowing to be used with open-source analysis tools.

5 Characterization of the Field-of-View Background Model

After having presented how the FoV background model was constructed, in this chapter the characteristics of the created model shall be examined. First the shape of the spatial background distribution will be investigated with regard to different energy and zenith/azimuth bins. After analyzing the spectra of the background rate for different observational bins it will be tested how well the model fits to a set of observational data. A selected set of H.E.S.S. I observational runs of PKS 2155-304 will be used to check the agreement of the model concerning different zenith angles and optical phases.

5.1 Spatial Background Distribution

In this section the shape of the spatial background distribution will be examined. Figure 5.1.1 shows four maps of the background model of the same observational bin but each for a different energy bin. These maps correspond to the background model created for a zenith angle $\theta \in [25, 35)^\circ$ and an azimuth angle $\varphi \in [90, 270)^\circ$, each depicting the varying γ-like background across the FoV. It becomes apparent that the shape of the distribution strongly changes with energy. For lower energies the background rate has its maximum at or close to the center of the FoV, steadily decreasing towards the edges. However the shape of the distribution changes distinctly towards higher energies with the forming of a central void and a ring-like structure of larger background rate around it.
One possible explanation for this transition could be the following. With increasing energy of a primary particle also the respective air shower increases in size and more Cherenkov light is emitted. Thus also the range in which the shower maximum has to be located in to allow for detection by a telescope increases. However with increasing lateral distance d_l between the shower maximum and the axis of the pointing direction of the telescope the elliptical image of the shower is located closer to the camera edges. This makes it more likely for a shower to be rejected due to the *local distance cut* (see section 3.3) which is applied to avoid truncated images. Considering an air shower with a certain d_l and an axis parallel to the pointing direction the resulting elliptical image is oriented in a way that the major axis intersects with the camera center. If one and the same shower had an axis

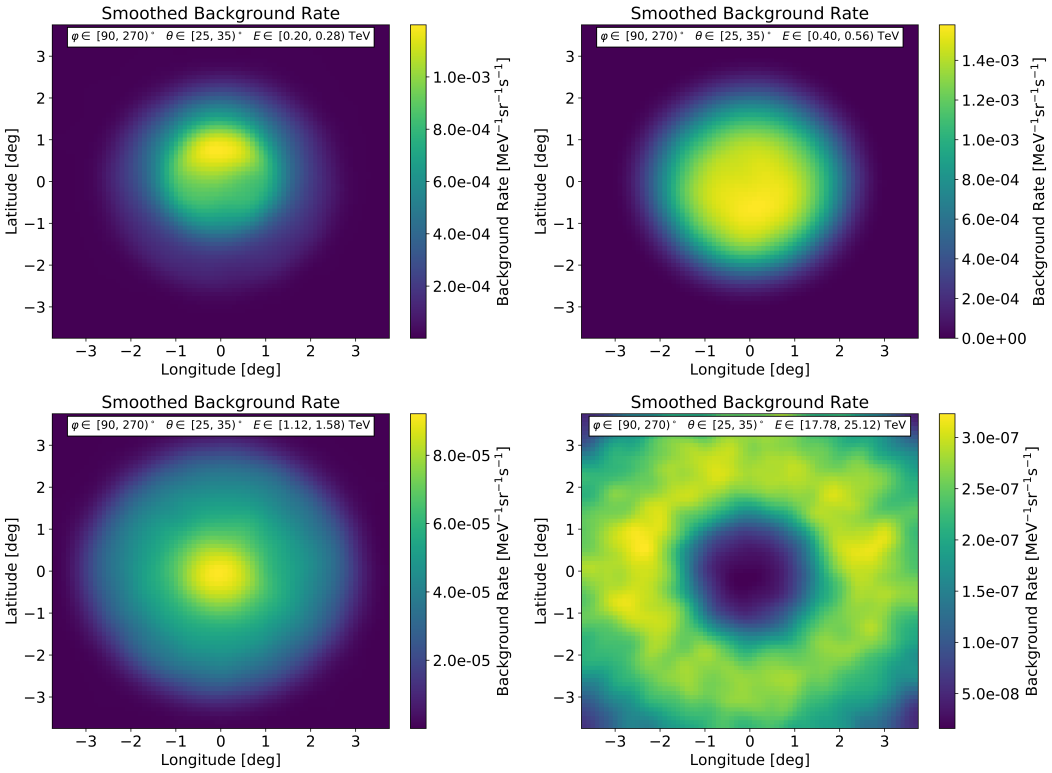

Figure 5.1.1: Background rate for different energy bins.

deviating from the pointing direction however the elliptical shower image would rotate inside the camera. Due to that rotation an ellipse previously too close to the camera edges or even partially out of bounds would now entirely fit into the camera and not be subject to the mentioned *local distance cut*.
Apart from the described effect there is another interesting behavior that becomes apparent when examining figure 5.1.1. In the very first energy bins the maximum background rate doesn't seem to be located in the center but rather being offset in positive latitude direction (top left). With increasing energies this maximum moves through the center then being positioned in negative latitude direction (top right). Eventually it reaches the center of the FoV (bottom left) followed by a smearing out effect and the formation of a central void (bottom right). This behavior is observed in every observational bin and can be both verified and quantified when determining the center of mass (COM) coordinates of the background maps for each energy bin. In figure 5.1.2 the latitude as well as the longitude of the COM coordinates is depicted for the first 5 zenith angle bins and azimuth angle bins 0 (top) and 1 (bottom).

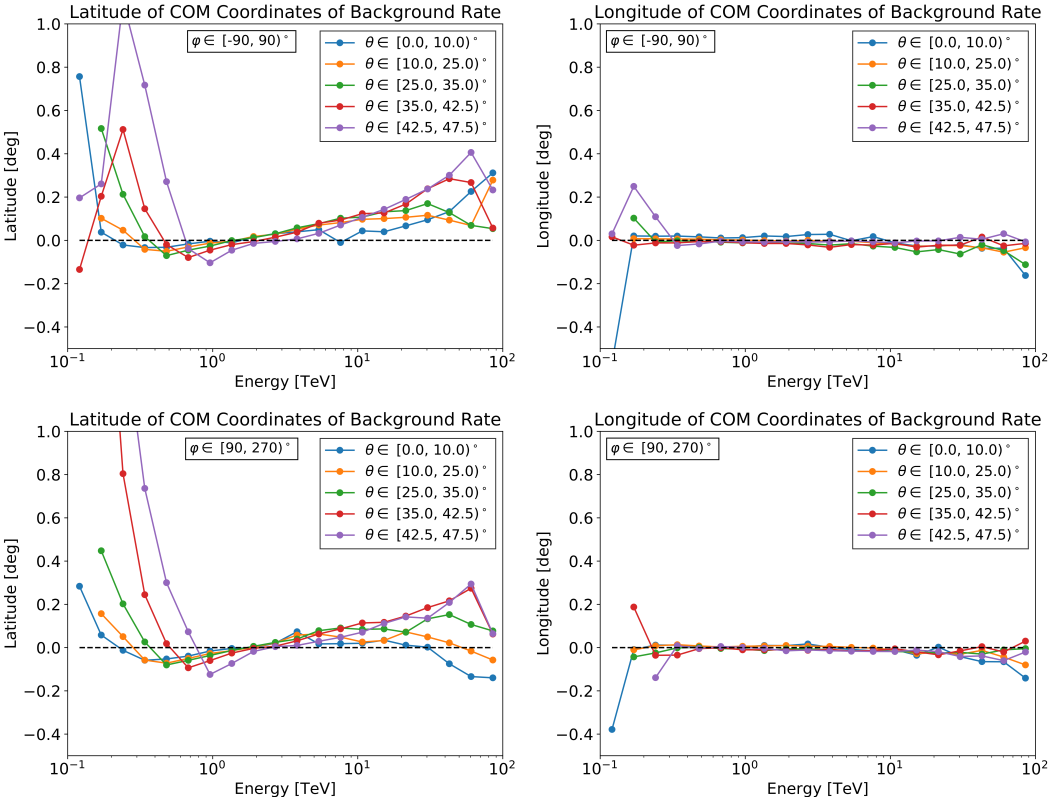

Figure 5.1.2: Center of mass coordinates of background rate for every energy bin. The energy values correspond to the center of the respective energy bin. **Top Left/Right:** Latitude/Longitude of COM coordinates per energy bin for $\varphi \in [-90, 90)^\circ$ and first 5 zenith angle bins. **Bottom Left/Right:** Latitude/Longitude of COM coordinates per energy bin for $\varphi \in [90, 270)^\circ$ and first 5 zenith angle bins.

When observing the development of the COM latitude component with increasing energies (top/bottom left) the behavior already observed in figure 5.1.1 is confirmed. Having positive values within the very first energy bins the curves all fall below zero with increasing energy until eventually approaching a value of zero at an energy of $\sim 2\,\text{TeV}$. This applies for every observational bin regardless of the azimuth angle. The initial deviation of the COM coordinates in positive latitude direction can be explained with the previously briefly mentioned zenith angle dependency of the low energy threshold. With a rising zenith angle the atmospheric depth for incident particles increases. This causes a loss in sensitivity to low energy air showers, resulting in a higher energy threshold [21]. Since the created background model is

represented in an Alt/Az-aligned FoV coordinate system a larger value in latitude corresponds to a larger value in altitude and thus a smaller zenith angle respectively. Consequently it is expected to register more events in positive latitude direction for energy bins close to the low energy threshold. Here it should be noted that each run within an observational bin has its own low energy threshold, usually defined as the value above which the energy bias (see section 3.2) is below 10%. These thresholds can vary despite having similar pointing concerning the zenith angle. Hence only energy bins above the one including the maximum low energy threshold among all runs can grant a fully trustworthy model. This of course is the most conservative approach possible but also the one maximizing the reliability of the created models. In table 5.1 the maximum low energy threshold among all runs within the same observational bin is listed each. As expected the energy threshold gets higher with increasing zenith bin number (i.e. higher zenith angles). This behavior applies for both azimuth bins likewise. It also becomes apparent that the observed shift of COM coordinates in positive latitude direction occurs at energies smaller than the maximum threshold of the respective energy bin in table 5.1. Hence it seems to be a valid assumption that this shift is an effect due to the zenith angle dependent energy threshold. The reason why the COM latitude component falls below zero and takes positive values again after approaching a value of zero at an energy of $\sim 2\,\mathrm{TeV}$ has yet to be explored.

		Zenith Bin									
		0	1	2	3	4	5	6	7	8	9
Azimuth	0	0.31	0.39	0.51	0.66	0.87	1.16	1.70	2.68	2.82	3.55
Bin	1	0.32	0.41	0.57	0.73	1.00	1.37	1.64	2.29	2.82	3.31

Table 5.1: Maximum low energy threshold in TeV among all runs within the respective observational bin.

When observing the development of the COM longitude component over rising energies (top/bottom right in figure 5.1.2) no distinct features can be recognized. All curves follow a similar path with values close to zero over the whole energy range. Since the longitude direction corresponds to the azimuth angle this is just as expected as there is no correlation between energy threshold and azimuth angle (see table 5.1).

5.2 Background Spectra

In this section the energy spectra of the created background model will be examined in detail. At first the spectrum of one specific observational bin shall be investigated more closely. Figure 5.2.1 shows three maps of the background model each

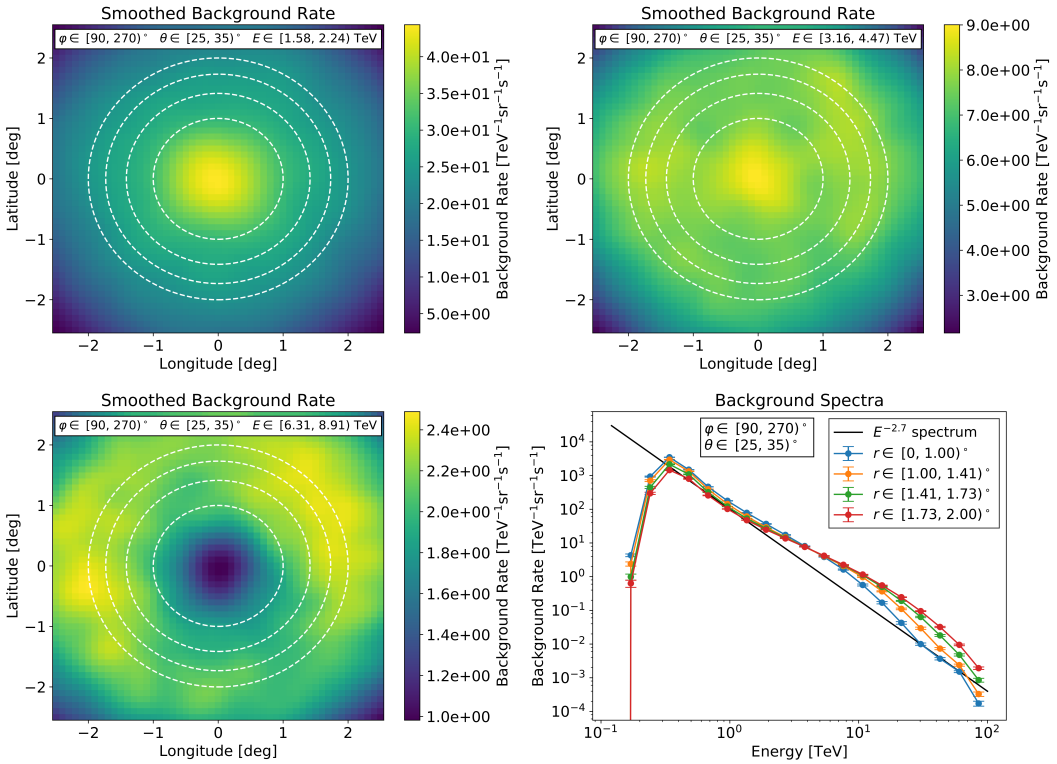

Figure 5.2.1: **Top Left/Right and Bottom Left:** Background rate for different energy bins with four concentric areas of the same size indicated by dashed white lines. **Bottom Right:** Background spectrum for each of the four areas over the whole energy range. The energy values correspond to the center of the respective energy bin.

for a different energy bin. Like in figure 5.1.1 these maps correspond to the observational bin with a zenith angle $\theta \in [25, 35)^\circ$ and an azimuth angle $\varphi \in [90, 270)^\circ$. Again they illustrate the previously mentioned smearing out effect towards higher energies eventually leading to a central void. Additionally four concentric areas are defined with their boarders represented by the dashed white lines. The radii of these circles are chosen to be equidistant in r^2 granting the same size for each of the resulting areas. For every energy bin the mean background rate of all the spatial pixels located inside the respective area was calculated. The resulting four spectra each representing one of these areas are depicted in figure 5.2.1 (bottom right).
The background rates for the very first energy bins can be ignored since they are too far below the low energy threshold and thus inconclusive. The rest of the spectrum looks like expected. For low energy bins the background rate inside the

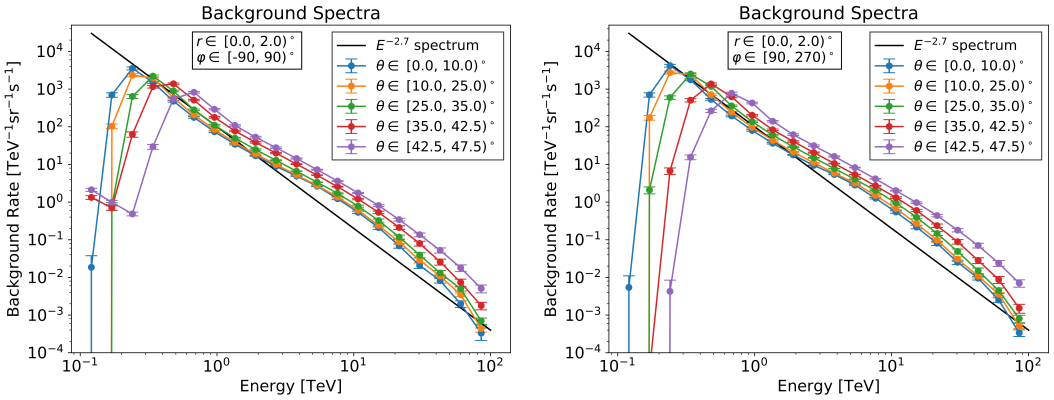

Figure 5.2.2: **Left:** Background spectra of first 5 zenith angle bins and $\varphi \in [-90, 90)°$. **Right:** Background spectra of first 5 zenith angle bins and $\varphi \in [90, 270)°$. To guide the eye, the black line shows a power law with index $\Gamma = 2.7$.

central area is the highest, steadily decreasing with increasing distance r to the center. At higher energies the opposite case is observed with the outermost area providing the highest background rate. Hence the four spectral curves are in total accordance with the previously made observations as they reflect the transition from a 2D Gaussian-like distribution to a ring-like structure around a central void. The exact same behavior is found when studying the spectra of other observational bins, proving to be a general characteristic being independent of zenith or azimuth angle.

Having verified the evolution of the spatial background distribution with increasing energy now the background spectra of several different observational bins shall be compared against each other. Instead of four spectra per observational bin just one spectrum was determined each. For every energy bin all spatial pixels inside a circular area with $r = 2°$ around the center were accounted for and used to calculate a mean background rate. Figure 5.2.2 shows the spectra of the first 5 zenith angle bins and azimuth angle bins 0 (left) and 1 (right).

When comparing the two different spectra (left and right) of the same zenith angle bin each hardly any differences can be identified. Independent of the respective azimuth angle bin all of the curves first rise with higher energies until reaching their maximum and then fall like a power law as a rough approximation. Besides the qualitative agreement the spectra also show a very good quantitative correspondence. Again the values for the very first energy bins are inconclusive as they are too far off the respective low energy threshold which is also the reason for the initial rise of the curves. As opposed to the azimuth angle bins distinct differences

are apparent when comparing the spectra of different zenith angle bins against each other. With increasing zenith bin number (i.e. greater zenith angles) the curves are shifted more and more towards higher energies until reaching their maximum each. As expected this once again demonstrates the already discussed zenith angle dependency of the low energy threshold (see section 5.1 and table 5.1). For higher zenith angles also the energy threshold increases. Above an energy of $\sim 0.7\,\mathrm{TeV}$ all curves have already reached their maximum and show a very similar shape despite being offset significantly. With increasing zenith bin number the offset in positive y-direction, and thus the background rate, becomes bigger. This behavior can be explained as follows. If a primary particle of a certain energy enters the atmosphere at the zenith the ensuing Cherenkov light cone will illuminate a circular area on the ground. However if the same particle was to enter the atmosphere under a zenith angle $\theta > 0$ the illuminated area on the ground would be of elliptical shape and inevitably bigger in size. Hence the higher the zenith angle of the incident particle also the larger the illuminated area on the ground. This makes it more likely for the telescopes to be located inside this area and thus detecting the event. Consequently for increasing zenith angles there is a higher chance for a primary particle to be registered resulting in a higher event rate.
On closer examination the spectra do not exactly follow a power law over the whole energy range but show a change in the spectral index each. Besides the calculated background spectra an additional curve with an index of $\Gamma = 2.7$ is plotted as a black line. This corresponds to the expected spectral index of cosmic rays within that energy range according to the previously shown all-particle spectrum (see figure 2.1.1). After having reached their maximum each the background spectra first fall linearly parallel to the $E^{-2.7}$ spectrum. Above an energy of $\sim 1.5\,\mathrm{TeV}$ however the curves become flatter with their spectral index changing to $\Gamma < 2.7$. This continues to an energy of $\sim 10\,\mathrm{TeV}$ above which the spectral index smoothly changes to $\Gamma > 2.7$ with the background spectra falling steeper again. One possible explanation for the changing spectral index could be a varying efficiency of the background suppression. Since the actual spectral index of cosmic rays is expected to be constant within the shown energy range the shape of the curves may be an indication of a first decreasing (until $\sim 10\,\mathrm{TeV}$) and then again increasing efficiency regarding the background rejection.
Besides the already discussed approach in section 5.1 it is worth mentioning at this point that there are also less conservative strategies to find the energy bin above which a trustworthy model can be ensured. One possibility for example is to check at which energy bin the spectrum of the respective observational bin reaches its maximum. From that energy bin on the model is expected to be valid. As opposed to the formerly mentioned approach this one isn't affected by single outliers resulting in more energy bins classified as reliable.

5.3 Agreement to PKS 2155-304 observational runs

In this section the agreement of the created background model with a set of observational data will be investigated. The data used for comparisons comprises a set of H.E.S.S. I runs observing PKS 2155-304 which is a point source and one of the brightest active galaxies in the sky. In total 90 different runs were selected and sorted regarding the zenith angle of their pointing as well as their optical phase. The latter represents the time window in which the observations were taken and accounts for the changing optical efficiency of the telescopes. Due to external circumstances the mirrors experience a degradation in sensitivity over time. The two optical phases taken into account were phase *1b* corresponding to all runs taken between 05/26/2004–07/03/2007 and phase *1c* corresponding to the observations done during 07/03/2007–04/27/2010. In phase *1b* all of the four telescopes had 70% of their nominal optical efficiency. This value dropped to 60% for three of the telescope in phase *1c* and to 54% for CT2. In table 5.2 the number of selected runs are listed concerning their optical phase and zenith angle. Due to the position of PKS 2155-304 all of the observations of this source have an azimuth angle $\varphi \in [90, 270)^\circ$. Each of the selected runs was done with all four telescopes being operational.

Zenith Angle [°]	0–20	20–30	30–40
Opt. Phase 1b	21	12	12
Opt. Phase 1c	21	12	12

Table 5.2: Number of selected PKS 2155-304 H.E.S.S. I observational runs per optical phase and zenith angle.

At first just one single run shall be examined, providing the motivation for the ensuing analysis. One way to check the agreement between the background model and an observational run is to compare the maps of observed event counts to those predicted by the model. Considering a well fitting background model these counts are expected to be in agreement apart from the spatial pixels in which the source is located. Since the event maps represent the probability of γ-like events of a certain energy being reconstructed at a certain position within the FoV they reflect the system acceptance. Figure 5.3.1 shows such an event map of both a specific PKS 2155-304 observational run (top left) and the corresponding background model (top right) over the whole energy range each. The dashed white horizontal and vertical lines define bands of 1.4° width providing slices for an illustrative one-dimensional comparison which is displayed in the bottom two plots. Here the projection of the event maps within these bands of both the data (red dots) and the corresponding background model (black line) along x- (left) and

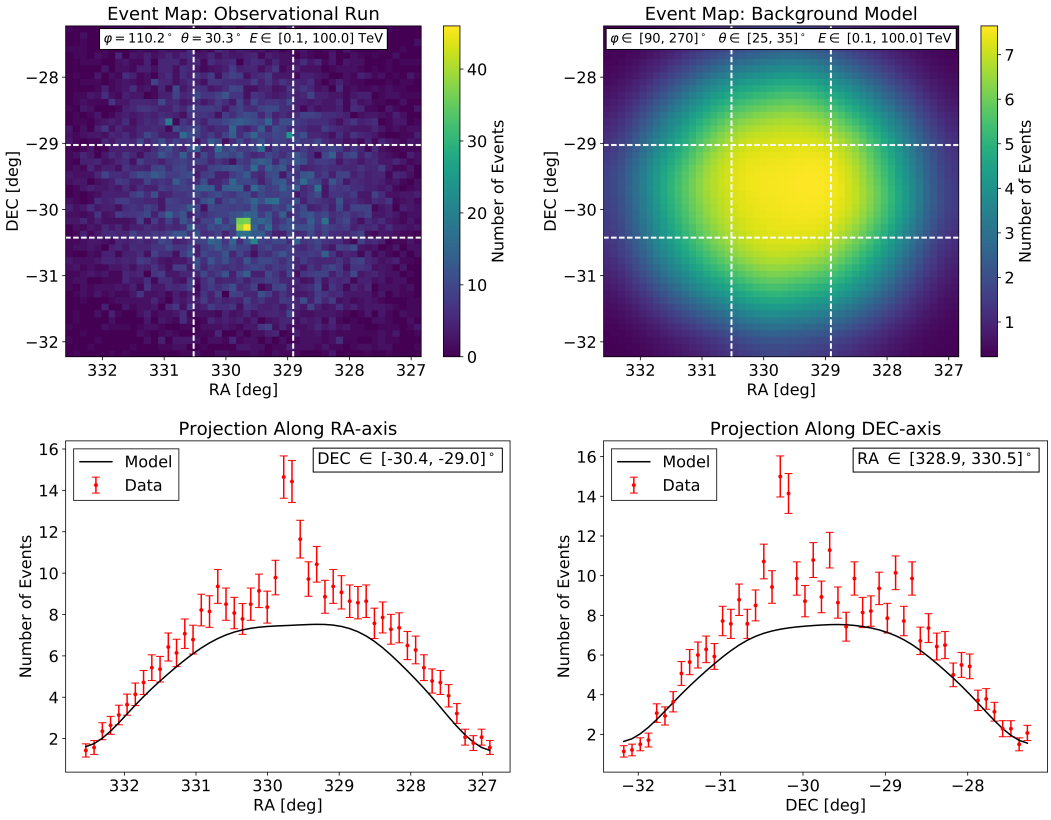

Figure 5.3.1: **Top Left/Right:** Event map over the whole energy range of one PKS 2155-304 observational run / the corresponding background model. The dashed white lines define bands providing slices for a one-dimensional comparison shown in the lower panel. **Bottom Left/Right:** Projection of both data and model along the x-/y-axis within the indicated band displayed in the upper panel.

y-direction (right) are depicted. The chosen observation was done with a pointing direction of $\theta = 30.3°$ in zenith and $\varphi = 110.2°$ in azimuth.
It should be noted that the used event maps are depicted in the equatorial coordinate system. Hence the x-direction corresponds to the right ascension angle (RA) and the y-direction corresponds to the declination angle (DEC). The advantage of using these RA/DEC coordinates is that the position of a point in the sky retains it coordinates over time. As will be seen later in this section this simplifies matters when it comes to cutting out the source for multiple different runs since its coordinates always stay the same in that system.
In figure 5.3.1 (bottom) there are two data points each which have a strong devia-

tion from the model. When having a look at the corresponding coordinates these points can be understood as a result of γ-ray events from PKS 2155-304. Apart from that the overall shape of the data points fits fairly well to the background model. Despite this relatively good qualitative agreement however the vast majority of the data points lies above the model. To quantify the agreement between the run data and the model a background normalization factor Φ can be determined. Multiplying the background model with Φ then represents the best fit to the actual data. Ideally a normalization of $\Phi = 1$ is expected as this value reflects a perfect fit of the model to the run data. Figure 5.3.1 serves as a good illustration of the importance of the normalization factor. For the shown scenario a normalization $\Phi > 1$ would be anticipated. By investigating Φ for multiple observations and every energy bin each valuable conclusions can be drawn concerning the quality of the created background model.
The ansatz chosen to determine the normalization factor in this thesis relies on the assumption of a Poisson distribution of the event rate for every spatial pixel. Therefore with the background model predicting λ_i events for the i-th spatial pixel the probability to measure a certain number of events inside that pixel N_i during an observational run is given by

$$P_i(N_i, \lambda_i) = \frac{\lambda_i^{N_i} e^{-\lambda_i}}{N_i!}. \tag{5.1}$$

By inserting the data from a certain run and the predictions from the corresponding background model the overall probability to obtain the measured data is given by the product of the single probabilities for each spatial pixel $P = \prod_i P_i(N_i, \lambda_i)$. This is where the background normalization factor comes into play again. By changing the parameter $\lambda_i \to \Phi\lambda_i$ in equation 5.1 the probability P_i and consequently P now also depend on the background normalization factor Φ. Since the values of both the observational run N_i and the background model λ_i are fixed one can adjust Φ in order to maximize P which can now be called a likelihood function. This so-called maximum likelihood estimation is a method which finds the value of Φ that maximizes the likelihood function and therefore selects the normalization factor that makes the observed data most probable. Due to the complex exponential terms working with the natural logarithm of the likelihood function, also called log-likelihood, is often more convenient. It simplifies the calculations and may be done since the location of the maximum does not change due to the monotony of the logarithm. Thus the normalization factor Φ for which the negative log-likelihood function, given by

$$-\ln(P) = -\sum_i \left[N_i \ln(\Phi\lambda_i) - \Phi\lambda_i - \ln(N_i!)\right], \tag{5.2}$$

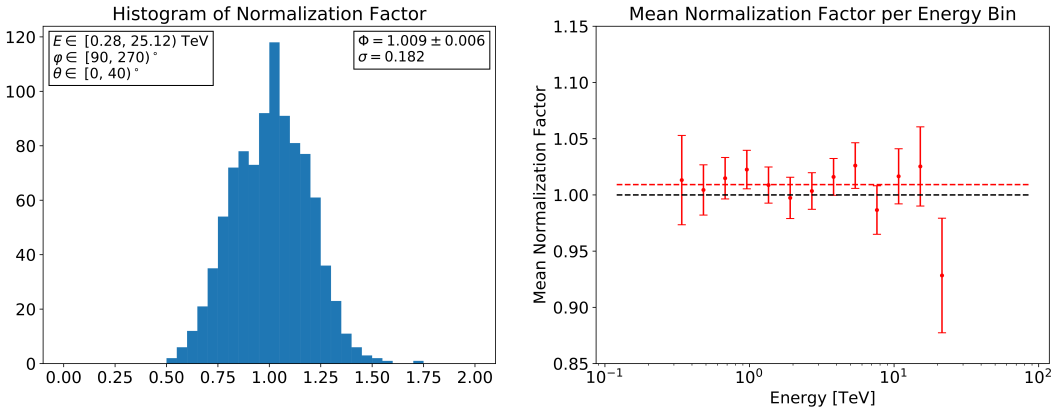

Figure 5.3.2: **Left:** Histogram of all calculated background normalization factors. **Right:** Plot of the mean normalization factor for each energy bin. To guide the eye, the dashed black represents the desired value of 1. The dashed red line corresponds to the determined mean value of Φ.

is minimized was determined. This was done for every of the 90 selected PKS 2155-304 observational runs and every energy bin each. To only account for γ-like background events all spatial pixels within a radius of 0.3° around the source position were excluded from those computations. Additionally all energy bins, in which less than a total of 25 events were predicted by the background model, were rejected to ensure a minimum level of statistics. Furthermore the low energy threshold was checked for every run and only the event maps of energy bins above the one including this energy threshold were taken into account. It should be noted that the last term in equation 5.2 was ignored in the calculations since it is just an offset that does not depend on Φ.
Figure 5.3.2 (left) shows the histogram of all 956 calculated background normalization factors. The distribution has a Gaussian-like shape as a rough approximation and is centered close to 1. The resulting mean value of the normalization factor is $\Phi = 1.009 \pm 0.006$ and thus in good agreement with the expected value of 1. On average the constructed background models seem to fit the observational data quite well. Figure 5.3.2 (right) displays the mean normalization factor for each energy bin (red dots). Most of these values lie slightly above 1, represented by the dashed black line. The just mentioned resulting mean value over all energy bins is depicted by the dashed red line. By investigating the histograms corresponding to the different optical phases and zenith angle intervals the origin of this slight deviation will be explored in the following.
In figure 5.3.3 (top/bottom left) the histograms of Φ stemming from all runs of optical phase *1b/1c* are displayed. With a total of 494 normalization factors cal-

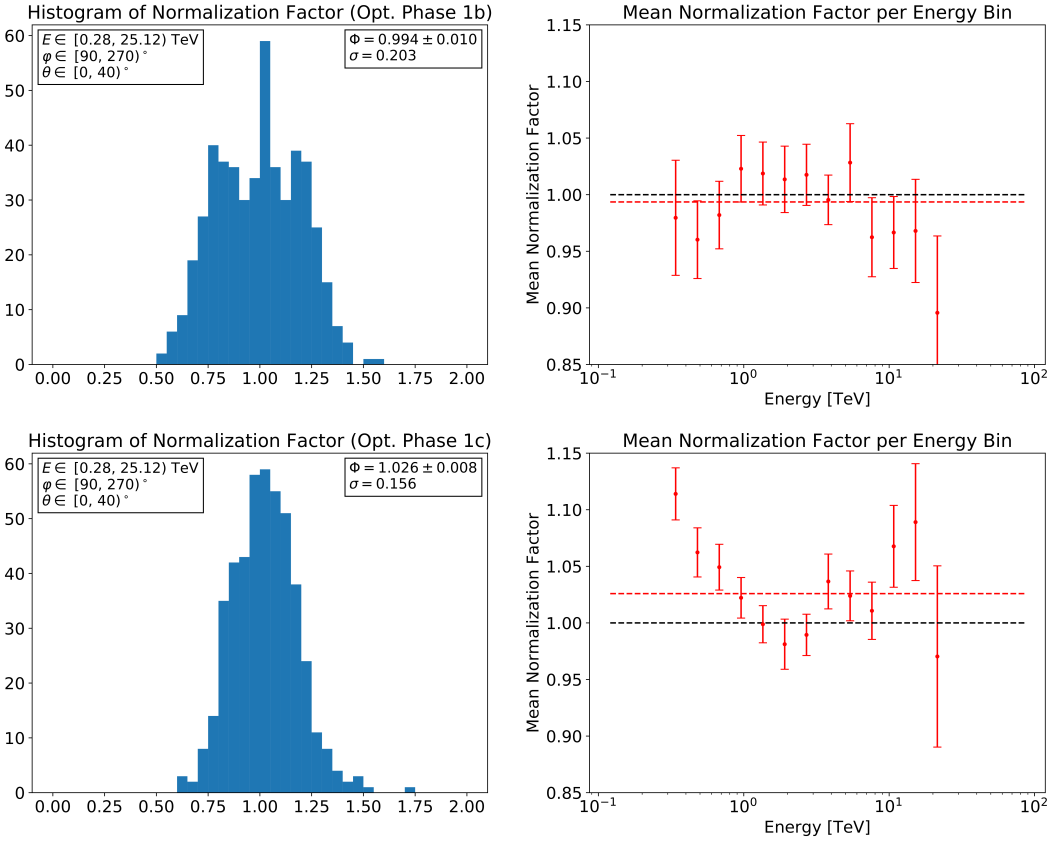

Figure 5.3.3: **Top/Bottom Left:** Histogram of calculated background normalization factors based on observational runs of optical phase *1b*/*1c*. **Top/Bottom Right:** Plot of the respective mean normalization factor for each energy bin.

culated for phase *1b* and 462 for phase *1c* the underlying statistics are roughly the same. For optical phase *1b* the mean value $\Phi_{1b} = 0.994 \pm 0.010$ is very close to the expected value of 1. The result for optical phase *1c* however is comparatively far off this value with $\Phi_{1c} = 1.026 \pm 0.008$. As outlined in section 4.2 the H.E.S.S. I observations used to build the background models were only grouped in bins of zenith and azimuth. Different optical phases were not taken into account. The deviation between Φ_{1b} and Φ_{1c} is an indication that adding a binning concerning the optical phase of the runs may be beneficial. Another notable difference between the two histograms lies in their shape. For optical phase *1b* the distribution seems to be distinctly broader compared to optical phase *1c*. This observation is confirmed by the computed standard deviation which can be found in the upper

right corner of the respective histogram. In addition the distribution of optical phase *1b* shows two local maxima around a central peak, whereas the distribution of phase *1c* rather follows a Gaussian-like shape. Figure 5.3.3 (top/bottom right) shows the mean normalization factor for each energy bin for the respective optical phase. Again the dashed black line represents a value of 1 and the dashed red line corresponds to the computed mean value over all energy bins. Most values for optical phase *1b* are relatively close to the expected value of 1. Starting with values < 1 the mean normalization gets greater with increasing energy bin number until eventually falling again. For phase *1c* the opposite behavior can be observed. First the mean normalization factor gets smaller with increasing energy bin number and then gets greater again after reaching values just below 1. It should be noted that the last value originates from rather few statistics and therefore has to be treated with caution. Due to the earlier mentioned rejection criteria only 9/7 of 45 runs were contributing to the calculations for optical phase *1b*/*1c* regarding that specific energy bin.

Now the histograms corresponding to the different zenith angle intervals shall be investigated more closely. In figure 5.3.4 (left) the distributions of the normalization factors for the respective zenith angles are displayed. It should be noted that the underlying data for zenith angles $\varphi \in [0, 20)^\circ$ (top) comprises 444 normalization factors, whereas only 254 and 258 normalizations were accounted for $\varphi \in [20, 30)^\circ$ (middle) and $\varphi \in [30, 40)^\circ$ (bottom) (see table 5.2). For the first zenith angle interval the mean value $\Phi_{0^\circ - 20^\circ} = 0.983 \pm 0.010$ lies slightly under the desired value of 1. The result for zenith angles $\varphi \in [20, 30)^\circ$ however varies quite widely from this value with $\Phi_{20^\circ - 30^\circ} = 1.045 \pm 0.010$. For the last zenith angle interval the mean value $\Phi_{30^\circ - 40^\circ} = 1.019 \pm 0.012$ is closer to 1 but also ranges above the expected value. These results are indicated as a dashed red line each in figure 5.3.4 (right) where the mean normalization factor is displayed per energy bin for the respective zenith angle interval each. Again also a dashed black line representing a value of 1 is plotted each which makes it easier to tell the discrepancies between this value and the respective calculated mean normalization factor.

In contrast to optical phases, varying zenith angles of the pointing direction were taken into account when building the background model. Thus the deviations may seem somewhat surprising. However they can be explained when having a closer look at the zenith bin boundaries which are $[0, 20, 30, 40]^\circ$ for the selected set of PKS 2155-304 observational data. The first zenith bin edges of the background model are $[0, 10, 25, 35, 42.5]^\circ$ (see table 4.1). This means that for all PKS 2155-304 observational runs with a zenith pointing angle $\theta \in [10, 20)^\circ$ the log-likelihood fit was done with a background model based on runs with a zenith pointing angle $\theta \in [10, 25)^\circ$. As seen in section 5.2 the event rate increases with increasing zenith angle above the respective low energy threshold. Thus the model assigned to those observational runs is based on runs that have a higher event rate on average as they

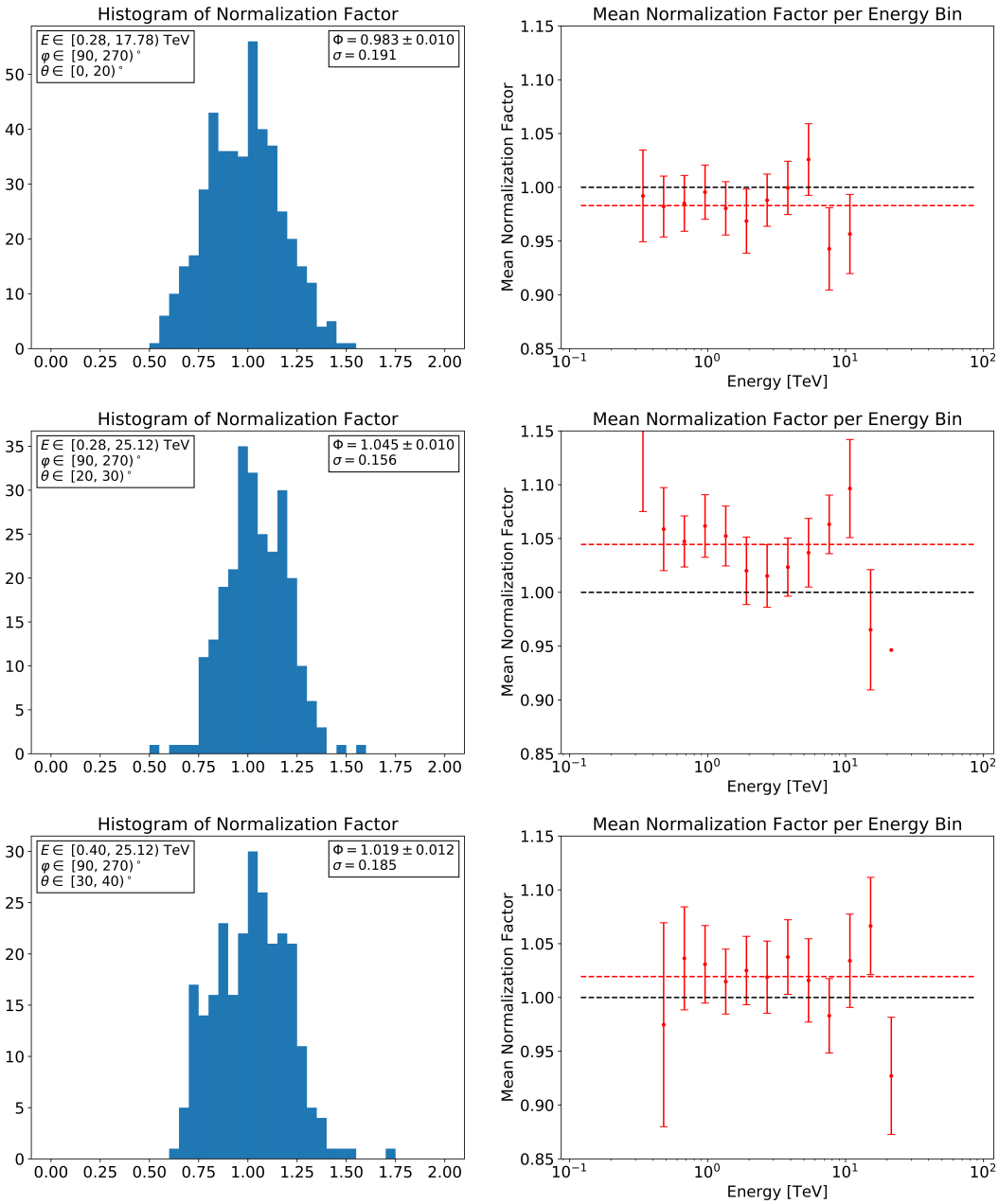

Figure 5.3.4: **Left:** Histogram of calculated background normalization factors based on observational runs with $\varphi \in [0, 20)^\circ$ (top), $\varphi \in [20, 30)^\circ$ (middle) and $\varphi \in [30, 40)^\circ$ (bottom). **Right:** Plot of the respective mean normalization factor for each energy bin.

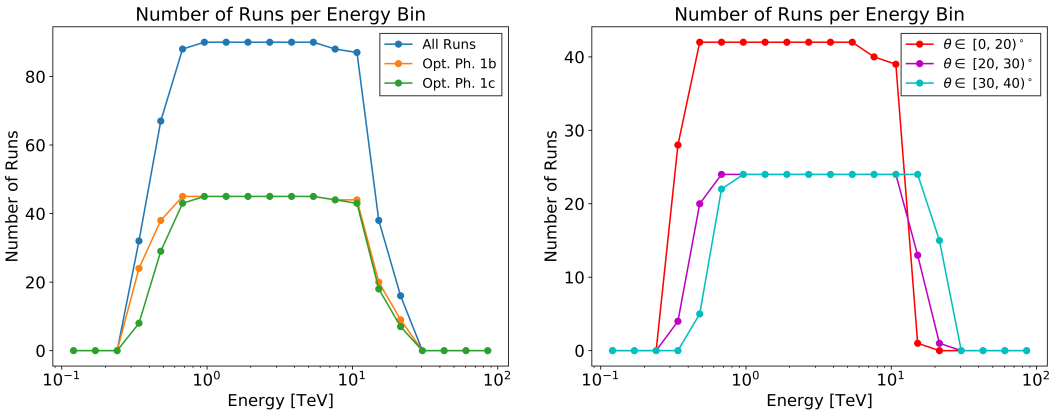

Figure 5.3.5: Number of runs contributing to the calculation of Φ within the respective energy bin.

have a higher zenith angle on average. As a consequence one obtains a background normalization factor $\Phi_{0°-20°} < 1$. When dealing with PKS 2155-304 observational runs with a zenith pointing angle $\theta \in [20, 30)°$ the opposite is the case. The assigned background model for all observational runs with $\theta \in [25, 30)°$ is based on runs with a zenith pointing angle $\theta \in [25, 35)°$. Thus the model relies on observations with zenith angles up to 5° greater than the observations in question. On the other hand the assigned model for all observational runs with $\theta \in [20, 25)°$ stems from runs with a zenith angle $\theta \in [10, 25)°$. Since these runs have a lower zenith angle on average also their event rate is lower on average which leads to a mean normalization factor greater than 1. This is the effect that dominates since in the latter case the model relies on observations with zenith angles up to 10° smaller compared to the PKS 2155-304 observational runs. Consequently the determined background normalization factor $\Phi_{20°-30°}$ is greater than 1. The exact same argumentation applies for the normalization factor $\Phi_{30°-40°}$ which is also greater than 1.
In figure 5.3.5 (left) the number of runs that contributed to the calculation of the normalization factor Φ within the respective energy bin is displayed for all runs (blue) and runs of optical phase *1b*/*1c* (orange/green). On the right the same curves are displayed for all runs corresponding to the different zenith angle interval each. The gradual initial increase of the curves in the left plot is a result of the already mentioned threshold criterion. Only energy bins above the one including the respective low energy threshold were taken into account for each run. Since the used data set comprises observational runs with zenith angles $\theta \in [0, 40)°$ and the threshold increases with higher zenith angles (see section 5.2) this explains the observed shape. This can be confirmed when observing the shapes of the plots

on the right. The curve corresponding to zenith angles $\theta \in [0, 20)^\circ$ (red) reaches its maximum first and the curve corresponding to $\theta \in [30, 40)^\circ$ (cyan) reaches its last. The decrease of the curves in the left plot can be explained with the applied criterion to ensure a minimum level of statistics by demanding a total of at least 25 predicted background events. As already mentioned in section 5.2 the event rate increases with higher zenith angles. Thus with increasing zenith angle this criterion applies only in higher energy bins. This is exactly the behavior that can be observed on the right again where the red curve falls earlier than the cyan one. When comparing the curves corresponding to the two different optical phases the overall shape is very similar. However during the initial increase the orange curve lies above the green one. This is due to the fact that in optical phase *1b* all of the four telescopes had a higher optical efficiency. Consequently on average more energy bins of runs taken in phase *1c* are affected by the threshold criterion than of runs done in phase *1b*.

6 Summary and Outlook

The subtraction of the background of cosmic-ray induced air showers is a major challenge for ground-based γ-ray telescope systems. Thus providing a proper model that gives an estimate of these background events is of crucial importance. There are several different types of background models like the ring or the reflected-region method for example. These two common techniques take a specific observational run and provide a background estimate for a certain on-region by using the data from the run itself. They are well applicable concerning γ-ray point sources, however they can often not be applied when dealing with complex field of views for which adequate off-regions cannot be defined. An alternative method is to construct a background model from numerous archival observations. Such a field-of-view (FoV) background model carries some additional systematics but offers great advantages when dealing with complicated field of views. It allows for background estimations for very extended sources, areas containing multiple overlapping sources and also regions with diffuse γ-ray emission like the Galactic plane. The aim of this master thesis was the development and characterization of such a FoV background model for the High Energy Stereoscopic System (H.E.S.S.).
The data used to create the model comprises 11986 observational runs of the H.E.S.S. experiment taken between 01/2004 and 06/2013 with a total observation time of 5265 h. To account for the varying system acceptance these runs were grouped in bins of zenith and azimuth angle, resulting in 26 different observational bins and thus eventually in 26 independent background models. All runs within the same observational bin were stacked by adding up all registered events in an Alt/Az-aligned FoV coordinate system. Events from known γ-ray sources were dismissed to only account for the γ-like background. Also the energy of the events was taken into consideration, resulting in a 3D histogram for every observational bin. Each of those histograms consists of several 2D background event maps corresponding to different energy bins. To obtain a bin content independent of the binning definition, a translation of the number of events per bin into a background rate in units of $\mathrm{MeV}^{-1}\mathrm{sr}^{-1}\mathrm{s}^{-1}$ was performed next. In order to remove statistical fluctuations a smoothing algorithm was applied on the obtained histograms. The resulting 26 unique 3D background models were stored in tables using the FITS format, making it possible to utilize them with open-source analysis tools.
The model was then studied with respect to its spatial and spectral characteristics. Its spatial shape is similar for each observational bin, but evolves strongly with

energy. For low energies the background rate maps show a 2D Gaussian-like distribution. With increasing energy a smearing out effect of the centered maximum can be observed, eventually leading to the formation of a ring-like structure around a central void. The energy spectrum of the model shows the expected characteristics. For every observational bin the spectrum approximately follows a power law with a spectral index close to $\Gamma = 2.7$, which corresponds to the index of the all-particle spectrum of cosmic rays within the considered energy range. A slight change of the spectral index is a phenomenon observed consistently in every observational bin and may be an indication of a varying efficiency of the applied background suppression. The spectra for different zenith angles are shifted with respect to each other due to the low energy threshold and the effective area increasing with zenith angle, as expected.
Finally, the agreement of the background model with a set of 90 PKS 2155-304 observational runs was investigated. By applying a log-likelihood fit an overall background normalization factor of $\Phi = 1.009 \pm 0.006$ was obtained, proving the model to fit well to the run data. The normalizations computed for runs from two phases with different optical efficiency of the telescopes (*1b* and *1c*) however show a slight deviation to one another. This is an indication that in the future it may be beneficial to add a binning concerning the optical efficiency of the runs. The normalizations computed for three different zenith angle intervals also show notable deviations. These however can be explained due to different zenith bin boundaries used for the model and the selected set of PKS 2155-304 observational data. By reducing the size of the zenith angle bins used for the created background model these effects could be diminished.
Further studies have yet to be made to check whether the current binning parameters (zenith and azimuth angle) are sufficient or new ones like the optical efficiency should be added. A finer binning always reduces the available statistics within one observational bin, leading to larger statistical fluctuations in turn. This should be kept in mind when potentially adding extra classifications of the runs or adjusting the bin sizes of the current parameters. Finding a reasonable compromise between a finer binning granting a more accurate fit to a run of interest and more statistics within each observational bin reducing the fluctuations is of great importance.

Bibliography

[1] F. Aharonian et al. H.E.S.S. observations of PKS 2155-304. *A&A*, 430(3):865–875, 2005.

[2] F. Aharonian et al. Observations of the Crab nebula with HESS. *A&A*, 457(3):899–915, 2006.

[3] D. Berge, S. Funk, and J. Hinton. Background modelling in very-high-energy gamma-ray astronomy. *A&A*, 466:1219–1229, 2007.

[4] K. Bernlöhr. Max-Planck-Institut für Kernphysik (MPIK), Heidelberg. `https://www.mpi-hd.mpg.de/hfm/CosmicRay/ChLight/ChLat`. Online: accessed on 03/07/2018.

[5] K. Bernlöhr. Simulation of Imaging Atmospheric Cherenkov Telescopes with CORSIKA and sim telarray. *Astropart. Phys.*, 30:149–158, 2008.

[6] K. Bernlöhr et al. The optical system of the H.E.S.S. imaging atmospheric Cherenkov telescopes, Part I: layout and components of the system. *Astropart. Phys.*, 20:111–128, 2003.

[7] W. Bietenholz. The most powerful particles in the Universe: a cosmic smash. *arXiv:1305.1346*, 2013.

[8] J. Bolmont et al. The camera of the fifth H.E.S.S. telescope. Part I: System description. *NIM A*, 761:46–57, 2014.

[9] M. de Naurois and D. Mazin. Ground-based detectors in very-high-energy gamma-ray astronomy. *C.R. Physique.*, 16:610–627, 2015.

[10] S. Funk. *A new population of very high-energy γ-ray sources detected with H.E.S.S. in the inner part of the Milky Way.* Dissertation, Ruprecht-Karls-Universität Heidelberg, 2005.

[11] S. Funk. Ground- and Space-Based Gamma-Ray Astronomy. *Annu. Rev. Nucl. Part. Sci.*, 65:245–277, 2015.

[12] S. Funk et al. The Trigger System of the H.E.S.S. Telescope Array. *Astropart. Phys.*, 22:285–296, 2004.

[13] T.K. Gaisser. *Cosmic Rays and Particle Physics*. Cambridge University Press, 1990.

[14] S. Heinz. *A Detailed Study of the Supernova Remnant RCW 86 in TeV γ-Rays*. Dissertation, Friedrich-Alexander-Universität Erlangen-Nürnberg, 2012.

[15] W. Heitler. *The Quantum Theory of Radiation*. Dover Publications, Inc. New York, 1954.

[16] V. F. Hess. Über Beobachtungen der durchdringenden Strahlung bei sieben Freiballonfahrten. *Z. Phys.*, 13:1084–1091, 1912.

[17] W. Hofmann et al. Comparison of techniques to reconstruct VHE gamma-ray showers from multiple stereoscopic Cherenkov images. *Astropart. Phys.*, 122:135–143, 1999.

[18] J. Holder. Atmospheric Cherenkov Gamma-ray Telescopes. *World Scientific Review Volume*, 2015. University of Delaware, Newark DE19716.

[19] C. Jahn. *Systematic Studies of an On-Off-Analysis of H.E.S.S. data in Search for a Signal from the Dark Matter Halo of the Milky Way*. Dissertation, Friedrich-Alexander-Universität Erlangen-Nürnberg, 2013.

[20] T.-P. Li and Y.-Q. Ma. Analysis methods for results in gamma-ray astronomy. *ApJ*, 272:317–324, 1983.

[21] M. Mayer. *Pulsar Wind Nebulae At High Energies: A Diverse Population and Exceptional Twins*. Dissertation, Universität Potsdam, 2014.

[22] M. Mayer. Private communication, 2016.

[23] C. Medina. H.E.S.S. Collaboration. `https://www.mpi-hd.mpg.de/hfm/HESS/pages/press/2012/HESS_II_first_light/images/Image_13.JPG`. Online: accessed on 03/11/2018.

Acknowledgments / Danksagung

An dieser Stelle möchte ich mich bei all jenen bedanken, die zum Gelingen dieser Arbeit beigetragen haben, insbesondere bei:

Prof. Dr. Stefan Funk für die Vergabe dieses interessanten Themas, die freundliche Aufnahme in seine Arbeitsgruppe sowie die hilfreichen Gespräche und die Betreuung dieser Masterarbeit.

Prof. Dr. Christopher van Eldik für die hilfreichen Diskussionen sowie die Übernahme des Zweitgutachtens.

Dr. Lars Mohrmann für eine immer offen stehende Tür und das Korrekturlesen meiner Arbeit. Mit seinem großen Engagement und seiner ständigen Hilfsbereitschaft hat er maßgeblich zum Gelingen dieser Arbeit beigetragen.

Meinen Bürokollegen **Max Schandri**, **Christian Kupfer** und **Kristof Kremer** für die angenehme Arbeitsatmosphäre und schöne Zeit mit vielen unterhaltsamen, auch manchmal weniger-fachlichen Gesprächen sowie die schnelle Hilfe bei Problemen und Fragen jeglicher Art.

Meinen Eltern **Christine** und **Alfred Sobel**, ohne deren Unterstützung weder mein Studium noch diese Arbeit möglich gewesen wären.

Erklärung

Hiermit versichere ich, dass ich diese Masterarbeit selbständig verfasst und keine anderen als die angegebenen Quellen und Hilfsmittel benutzt habe. Die Stellen meiner Arbeit, die dem Wortlaut oder dem Sinn nach anderen Werken entnommen sind, habe ich in jedem Fall unter Angabe der Quelle als Entlehnung kenntlich gemacht. Das selbe gilt sinngemäß für Tabellen und Abbildungen. Diese Arbeit hat in dieser oder einer ähnlichen Form noch nicht im Rahmen einer anderen Prüfung vorgelegen.

Erlangen, den 9. Mai 2018 .....
Christopher Sobel